

Hydrodynamics of a weakly curved channel

Cite as: Phys. Fluids **31**, 055110 (2019); <https://doi.org/10.1063/1.5098827>

Submitted: 04 April 2019 . Accepted: 01 May 2019 . Published Online: 23 May 2019

Sk Zeeshan Ali , and Subhasish Dey 



View Online



Export Citation



CrossMark

ARTICLES YOU MAY BE INTERESTED IN

[Referee acknowledgment for 2018](#)

Physics of Fluids **31**, 020201 (2019); <https://doi.org/10.1063/1.5090536>

[Geometric optimization of riblet-textured surfaces for drag reduction in laminar boundary layer flows](#)

Physics of Fluids **31**, 053601 (2019); <https://doi.org/10.1063/1.5090881>

[Image processing for bubble morphology characteristics in diluted bubble swarms](#)

Physics of Fluids **31**, 053306 (2019); <https://doi.org/10.1063/1.5088945>



CAPTURE WHAT'S POSSIBLE
WITH OUR NEW PUBLISHING ACADEMY RESOURCES

Learn more 



Hydrodynamics of a weakly curved channel

Cite as: Phys. Fluids 31, 055110 (2019); doi: 10.1063/1.5098827

Submitted: 4 April 2019 • Accepted: 1 May 2019 •

Published Online: 23 May 2019



Sk Zeeshan Ali^{1,a)}  and Subhasish Dey^{1,2,3,b)} 

AFFILIATIONS

¹Department of Civil Engineering, Indian Institute of Technology Kharagpur, Kharagpur, West Bengal 721302, India

²Physics and Applied Mathematics Unit, Indian Statistical Institute Kolkata, Kolkata, West Bengal 700108, India

³Department of Hydraulic Engineering, State Key Laboratory of Hydro-Science and Engineering, Tsinghua University, Beijing 100084, China

^{a)}skzeeshanali@iitkgp.ac.in

^{b)}Author to whom correspondence should be addressed: sdey@iitkgp.ac.in

ABSTRACT

The underlying mechanism of curvature induced helicoidal flow in a weakly curved channel intrigues researchers. Here, we explore the hydrodynamics of weakly curved channels, defined by the limiting values of the curvature ratio (ratio of channel half-width to radius of curvature) and aspect ratio (ratio of channel half-width to average flow depth) as 0.1 and 10, respectively. The three-dimensional continuity and momentum equations are solved analytically, involving the appropriate boundary conditions and closing the system by means of the turbulence closure model and the indispensable fluid constitutive formulations. The skewed filament of the azimuthal velocity component, emanating from the effects of curvilinear streamlines, is introduced into the analysis, for the first time, to address the flow asymmetry across the flow cross section. The modification of the radial slope due to the presence of the stress term in the radial momentum balance is accomplished by a slope correction factor, which turns out to be a weak function of the reciprocal of the power-law exponent. The attenuation of the azimuthal shear stress component, resulting from the skewed velocity profile, is characterized by the damping function to provide a quantitative insight into the redistribution of the primary flow momentum. The velocity field reveals that the flow circulation (on the flow cross-sectional plane) about the azimuthal axis and the flow helicity strengthen with an increase in the curvature ratio. The variation of the radial free surface profile is more sensitive to the flow Froude number than to the curvature ratio. The evolutions of the stress field with several key parameters are also examined.

Published under license by AIP Publishing. <https://doi.org/10.1063/1.5098827>

I. INTRODUCTION

The flow in a curved channel remains one of the fascinating and sparking topics of classical fluid dynamics. Owing to the profound effects of curvilinear streamlines on many natural and industrial flows, the subject has been largely studied in the past decades not only from the perspective of intrinsic scientific rationales but also from the standpoint of ample engineering applications. In this context, it is worth highlighting that Dean^{1,2} was the pioneer to analytically solve the laminar flow in a weakly curved pipe. Momentous advances in experimental techniques and numerical simulations to analyze the flow in a curved pipe were reviewed elsewhere.³ This study, however, puts into focus the flow in a weakly curved open channel. Modeling of flow, in particular, in a curved channel has so far received a lot of attention, in quest of new motifs to smoothly maneuver a channel flow. In the realm of hydrodynamics, accurate estimations of velocity and bed shear stress components, even for

the most simplified flow geometry, are the central prerequisite to assess the stability of a natural riverbed. Moreover, the topic has far-reaching applications from the environmental perspective, for instance in anticipating the dispersion of nutrients and pollutants in a fluvial system.⁴ Before going into the relevant literature survey on the topic, a succinct description of the underlying mechanism of a curved channel flow is furnished below.

When a fluid flows in a curved channel, the primary flow is affected owing to the centrifugal acceleration, leading to the secondary current of Prandtl's first kind, which results from the skewing of the mean flow due to the curvilinear streamlines.^{5,6} The secondary current, in conjunction with the primary flow, form a helicoidal motion that evolves in three dimensions. The helicoidal flow eventually attains an equilibrium state, recognized as the fully developed flow, in which the flow structure does not alter from one cross section to another. The helicoidal motion can be readily envisaged as a secondary circulation across a given cross-sectional area

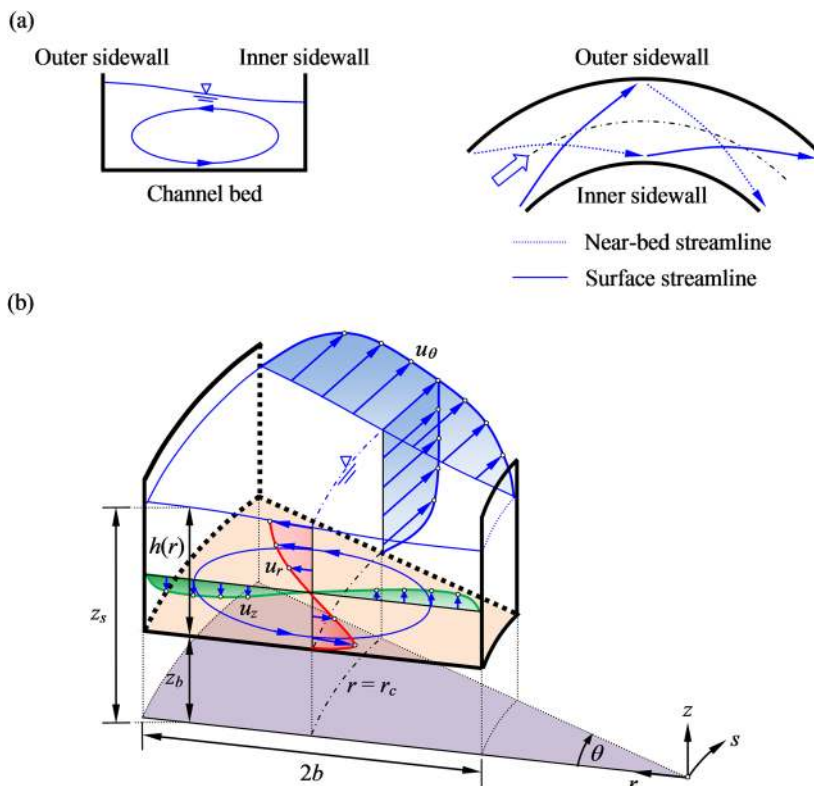


FIG. 1. Schematic illustration of flow in a weakly curved channel: (a) cross-sectional and plan views and (b) three-dimensional velocity components (u_r , u_θ , u_z) in a cylindrical polar coordinate system (r , θ , z). Here, b is the channel half-width, $h(r)$ is the local flow depth at a radial distance r , r_c is the radius of curvature of the channel centerline, s is the azimuthal distance given by $r\theta$, θ is the azimuthal angle, and z_b and z_s are the elevations of the channel bed and the free surface, respectively.

[Fig. 1(a)]. The emergence of the secondary circulation is inextricably linked with the differential centrifugal acceleration over the entire vertical fluid column, resulting from the vertical variation of the azimuthal velocity. It follows that the centrifugal acceleration is maximum at the free surface, while it reduces toward the bed. This leads to a fluid motion being radially outward, transporting and amassing the fluid toward the outer sidewall. In consequence, there appears a striking phenomenon, called the super-elevated free surface, implying that the free surface elevation at the outer sidewall exceeds that at the inner sidewall [Fig. 1(a)]. To partially balance the centrifugal force, a radial pressure gradient is generated, giving rise to a radial force that acts toward the inner sidewall. Under hydrostatic pressure assumption, the radial pressure gradient is linearly scaled with the radial free surface slope, revealing that at a given radial distance, the radial force remains constant over the entire flow depth. On the contrary, at a given radial distance, the centrifugal force significantly varies with the vertical distance owing to the differential azimuthal velocity. Thus, the imbalance between the centrifugal force and the radial force triggers a net radial force, which changes its sign at a specific vertical distance, leaving a generic signature of the origin of secondary circulation. Another consequence of the secondary circulation is that the near-bed streamlines are swerved toward the inner sidewall, while the surface streamlines are directed toward the outer sidewall [Fig. 1(b)].

A plethora of studies was reported in the past years to grasp the flow field in a curved channel. Including the earlier pioneering studies on the topic,^{7–10} the state-of-the-art of flow in a curved channel was thoroughly reviewed by Rozovskii¹¹ and Falc3n.¹² There

remain several analytical studies that were primarily dedicated to the flow field and bed topography in a curved channel.^{13–17} Importantly, the flow structure in the vertical direction was mostly studied either by solving the momentum equations or by employing the moment of momentum equations.^{11,14,18,19} Myriads of experimental and field studies were reported to explore the flow and turbulence characteristics in both weakly and strongly curved channels.^{20–27} Besides, several numerical experiments were conducted to simulate the flow structure in a curved channel.^{28–32} Specifically, a few models, based on the depth-averaged assumptions, were developed to study the flow and sediment dynamics in a curved channel.^{16,33,34} However, these depth-averaged models fall short to vividly represent the most essential elements of the helicoidal flow, for instance, the flow structure in the vertical direction and the secondary circulation.

Although there remain significant studies stemming from a rich heritage of analytical, experimental, and numerical frameworks, several key questions are yet to be answered, at least analytically, concerning even with the most fundamental problem of flow in a weakly curved channel. Some of these questions include how does an asymmetrical radial profile of azimuthal velocity affect the velocity and the shear stress fields in a curved channel; how could an encouraging theoretical foundation be developed to unravel the innate response of a weakly curved channel flow to the key parameters; which are the parameters that principally govern the evolutions of secondary circulation and the flow helicity; and what are the exact dependencies of the free surface profile on the key parameters. Despite several attempts,^{6,11} the sensitivity of the helicoidal flow structure

in a weakly curved channel flow to the key parameters is largely unknown analytically. It is worth mentioning that in most of the analytical studies, the radially skewed (asymmetry across the channel centerline) azimuthal velocity was surprisingly overlooked.^{11,14,23,35} This strong assumption can afflict the analysis since the azimuthal velocity must be radially skewed from the fundamental tenet of curvilinear flow in a curved channel, as is evident from experimental observations and numerical simulations.^{11,22,29} Therefore, precise determinations of velocity and shear stress components essentially require an asymmetrical radial profile of azimuthal velocity to mimic most of the real flow situation. The subtle role of the centrifugal acceleration in supervising the radial free surface profile is well-recognized.⁶ Nevertheless, little is known about how the free surface profile is precisely controlled by the flow Froude number and the curvature ratio. Although the redistribution of the primary flow momentum owing to the secondary circulation in a curved channel has been well documented,²⁹ its impact on the velocity and stress fields has so far been scarcely studied. In addition, the variations of secondary circulation and flow helicity in a curved channel with the curvature ratio remain unexplored from the analytical perspective.

This study therefore aims at exploring the flow field in a weakly curved channel by analytically solving the continuity and the momentum equations, to seek the basic response of the flow to the key parameters. In the theoretical analysis, the weak curvature approximations are sought, facilitating a promising framework that effectively solves the set of governing equations by entreating the turbulence closure relationships and the appropriate boundary conditions. The effects of curvilinear streamlines on the azimuthal velocity are addressed by considering a radially skewed profile of depth-averaged azimuthal velocity. The imbalance between the centrifugal force and the radial force is addressed by the radial slope correction factor. The reduction in the azimuthal shear stress owing to curvilinear streamlines is explicitly considered by introducing the damping function.

The paper is structured as follows. In Sec. II, the theoretical analysis is presented. Starting with the set of governing equations and the boundary conditions (Sec. II A), the modeling strategies together with the constitutive formulations are described (Sec. II B). Then, the radial free surface profile (Sec. II C), radial slope correction factor (Sec. II D), damping function (Sec. II E), and flow circulation about azimuthal axis and flow helicity (Sec. II F) are deduced. The model results are emphasized in Sec. III, including the velocity field (Sec. III A), radial free surface profile (Sec. III B), and stress field (Sec. III C). Finally, conclusions are drawn in Sec. IV, enlightening a brief description of the proposed methodology and a summary of the important results.

II. THEORETICAL ANALYSIS

The physical system of this study describes an incompressible fluid motion in a weakly curved rigid channel, having a rectangular cross section of constant width $2b$ [Fig. 1(c)]. In fact, a rectangular channel is classically treated as the most fundamental channel cross section because the actual cross sectional shape of a natural channel is arbitrary. To analyze the flow field, a cylindrical polar coordinate system (r, θ, z) is considered, where r is the radial distance from the center of curvature, θ is the azimuthal angle along the channel

centerline given by s/r , s is the azimuthal distance, and z is the vertical distance from a fixed horizontal plane. Let the radius of curvature of the channel centerline be r_c . We define the curvature ratio of the channel as $C = b/r_c$, being of the order of 0.1 ($C \leq 0.1$). In the schematic illustration [Fig. 1(c)], the elevations of the channel bed and the free surface are denoted by $z = z_b$ and z_s , respectively. Thus, the local flow depth at a radial distance r is given by $h(r) = z_s - z_b$. We define the aspect ratio of channel flow as $\mathcal{A} = b/\langle h \rangle$, where $\langle h \rangle$ is the average flow depth over the flow cross section. The channel width is considered to be much larger than the average flow depth, specifically $\mathcal{A} \geq 10$, in order to avoid the dip phenomenon.

A. Governing equations

The continuity and the momentum equations for an incompressible fluid in the cylindrical polar coordinate system (r, θ, z) read

$$\frac{1}{r} \frac{\partial(ru_r)}{\partial r} + \frac{1}{r} \frac{\partial u_\theta}{\partial \theta} + \frac{\partial u_z}{\partial z} = 0, \quad (1a)$$

$$\frac{Du_r}{Dt} - \frac{u_\theta^2}{r} = f_r - \frac{1}{\rho} \frac{\partial p}{\partial r} + v \left(\nabla^2 u_r - \frac{u_r}{r^2} - \frac{2}{r^2} \frac{\partial u_\theta}{\partial \theta} \right), \quad (1b)$$

$$\frac{Du_\theta}{Dt} + \frac{u_\theta u_r}{r} = f_\theta - \frac{1}{\rho r} \frac{\partial p}{\partial \theta} + v \left(\nabla^2 u_\theta - \frac{u_\theta}{r^2} + \frac{2}{r^2} \frac{\partial u_r}{\partial \theta} \right), \quad (1c)$$

$$\frac{Du_z}{Dt} = f_z - \frac{1}{\rho} \frac{\partial p}{\partial z} + v \nabla^2 u_z, \quad (1d)$$

where \mathbf{u} is the velocity vector ($=u_r, u_\theta, u_z$), t is the time, \mathbf{f} is the body force vector per unit mass density of fluid ($=f_r, f_\theta, f_z$), ρ is the mass density of fluid, p is the static pressure intensity, v is the coefficient of kinematic viscosity of fluid, and the operators D/Dt and ∇^2 are as follows:

$$\frac{D}{Dt} = \frac{\partial}{\partial t} + u_r \frac{\partial}{\partial r} + \frac{u_\theta}{r} \frac{\partial}{\partial \theta} + u_z \frac{\partial}{\partial z}, \quad (1e)$$

$$\nabla^2 = \frac{\partial^2}{\partial r^2} + \frac{1}{r} \frac{\partial}{\partial r} + \frac{1}{r^2} \frac{\partial^2}{\partial \theta^2} + \frac{\partial^2}{\partial z^2}. \quad (1f)$$

The above set of governing equations can be simplified by applying the weak curvature approximation. To this end, we consider the characteristic length scale to be the radius of curvature of the channel centerline r_c and the characteristic time scale to be r_c/U_m , where U_m is the maximum flow velocity. Under such considerations, we introduce the following nondimensional variables:

$$\tilde{t} = t \frac{U_m}{r_c}, \quad \tilde{r} = \frac{r}{r_c}, \quad \tilde{z} = \frac{z}{r_c}, \quad (\tilde{u}_r, \tilde{u}_\theta, \tilde{u}_z) = \frac{(u_r, u_\theta, u_z)}{U_m}, \quad (2)$$

$$(\tilde{f}_r, \tilde{f}_\theta, \tilde{f}_z) = (f_r, f_\theta, f_z) \frac{r_c}{U_m^2}, \quad \tilde{p} = \frac{p}{\rho U_m^2}.$$

We also define $\varepsilon = h/r_c$ ($\ll 1$). Since $r = \mathcal{O}(r_c)$, $z = \mathcal{O}(h)$, $u_\theta = \mathcal{O}(U_m)$, and $p = \mathcal{O}(\rho U_m^2)$, it follows that $\tilde{r} = \mathcal{O}(1)$, $\tilde{z} = \mathcal{O}(\varepsilon)$, $\tilde{u}_\theta = \mathcal{O}(1)$, and $\tilde{p} = \mathcal{O}(1)$. In addition, experimental observations in weakly curved channels evidenced that $\tilde{u}_r = \mathcal{O}(\varepsilon)$.^{11,23} However, exact orders of magnitude of θ and u_z can be obtained from the

continuity equation [Eq. (1a)]. Substituting Eq. (2) into Eqs. (1a)–(1d) and performing the order of magnitude analysis yield

$$\frac{1}{\tilde{r}} \frac{\partial(\tilde{r}\tilde{u}_r)}{\partial\tilde{r}} + \frac{1}{\tilde{r}} \frac{\partial\tilde{u}_\theta}{\partial\theta} + \frac{\partial\tilde{u}_z}{\partial\tilde{z}} = 0, \quad (3a)$$

$$\frac{\partial\tilde{u}_r}{\partial\tilde{t}} + \tilde{u}_r \frac{\partial\tilde{u}_r}{\partial\tilde{r}} + \frac{\tilde{u}_\theta}{\tilde{r}} \frac{\partial\tilde{u}_r}{\partial\theta} + \tilde{u}_z \frac{\partial\tilde{u}_r}{\partial\tilde{z}} - \frac{\tilde{u}_\theta^2}{\tilde{r}} = \tilde{f}_r - \frac{\partial\tilde{p}}{\partial\tilde{r}} + \frac{1}{R_N} \left(\frac{\partial^2\tilde{u}_r}{\partial\tilde{r}^2} + \frac{1}{\tilde{r}} \frac{\partial\tilde{u}_r}{\partial\tilde{r}} + \frac{1}{\tilde{r}^2} \frac{\partial^2\tilde{u}_r}{\partial\theta^2} + \frac{\partial^2\tilde{u}_r}{\partial\tilde{z}^2} - \frac{\tilde{u}_r}{\tilde{r}^2} - \frac{2}{\tilde{r}^2} \frac{\partial\tilde{u}_\theta}{\partial\theta} \right), \quad (3b)$$

$$\frac{\partial\tilde{u}_\theta}{\partial\tilde{t}} + \tilde{u}_r \frac{\partial\tilde{u}_\theta}{\partial\tilde{r}} + \frac{\tilde{u}_\theta}{\tilde{r}} \frac{\partial\tilde{u}_\theta}{\partial\theta} + \tilde{u}_z \frac{\partial\tilde{u}_\theta}{\partial\tilde{z}} + \frac{\tilde{u}_\theta\tilde{u}_r}{\tilde{r}} = \tilde{f}_\theta - \frac{1}{\tilde{r}} \frac{\partial\tilde{p}}{\partial\theta} + \frac{1}{R_N} \left(\frac{\partial^2\tilde{u}_\theta}{\partial\tilde{r}^2} + \frac{1}{\tilde{r}} \frac{\partial\tilde{u}_\theta}{\partial\tilde{r}} + \frac{1}{\tilde{r}^2} \frac{\partial^2\tilde{u}_\theta}{\partial\theta^2} + \frac{\partial^2\tilde{u}_\theta}{\partial\tilde{z}^2} - \frac{\tilde{u}_\theta}{\tilde{r}^2} + \frac{2}{\tilde{r}^2} \frac{\partial\tilde{u}_r}{\partial\theta} \right), \quad (3c)$$

$$\frac{\partial\tilde{u}_z}{\partial\tilde{t}} + \tilde{u}_r \frac{\partial\tilde{u}_z}{\partial\tilde{r}} + \frac{\tilde{u}_\theta}{\tilde{r}} \frac{\partial\tilde{u}_z}{\partial\theta} + \tilde{u}_z \frac{\partial\tilde{u}_z}{\partial\tilde{z}} = \tilde{f}_z - \frac{\partial\tilde{p}}{\partial\tilde{z}} + \frac{1}{R_N} \left(\frac{\partial^2\tilde{u}_z}{\partial\tilde{r}^2} + \frac{1}{\tilde{r}} \frac{\partial\tilde{u}_z}{\partial\tilde{r}} + \frac{1}{\tilde{r}^2} \frac{\partial^2\tilde{u}_z}{\partial\theta^2} + \frac{\partial^2\tilde{u}_z}{\partial\tilde{z}^2} \right), \quad (3d)$$

where R_N is $U_m r_c / \nu$ ($\gg 1$).

Equation (3a) reveals that since $\tilde{r} = \mathcal{O}(1)$, $\tilde{z} = \mathcal{O}(\epsilon)$, and $\tilde{u}_r = \mathcal{O}(\epsilon)$, the orders of magnitude of θ and \tilde{u}_z must be $\theta = \mathcal{O}(\epsilon^{-1})$ and $\tilde{u}_z = \mathcal{O}(\epsilon^2)$. The possible explanation for θ to be large [= $\mathcal{O}(\epsilon^{-1})$] is that the channel is weakly curved, and therefore, a change in velocity occurs on large scales of θ . Besides, as the local acceleration term must be of the same order of magnitude of the associated convective acceleration terms, Eq. (3b) suggests that the order of magnitude of \tilde{t} should be $\tilde{t} = \mathcal{O}(\epsilon^{-1})$. Therefore, in the left-hand side of Eq. (3b), all the terms except the last one [= $\mathcal{O}(1)$] can be ignored. On the other hand, the fourth term [= $\mathcal{O}(\epsilon^{-1})$] within the parentheses is much larger than the remaining terms. Hence, they can be dropped because R_N is a large number. Equation (3b) suggests that R_N should be of the order of $R_N = \mathcal{O}(\epsilon^{-1})$. In a similar way, in Eq. (3c), the terms in the left-hand side [= $\mathcal{O}(\epsilon)$] cannot be ignored, while the terms within the parentheses, except the fourth term [= $\mathcal{O}(\epsilon^{-2})$], are trivial. This indicates that R_N should be of the order of $R_N = \mathcal{O}(\epsilon^{-3})$. Here, one should not be confused with two different orders of magnitude of R_N as $R_N = \mathcal{O}(\epsilon^{-1})$ and $\mathcal{O}(\epsilon^{-3})$, anticipated from Eqs. (3b) and (3c), respectively, because for both the cases, another variable R_h ($= U_m h / \nu$) is adjusted spontaneously in such a way in order to keep the R_h / R_N ratio as a constant of

ϵ ($= h / r_c$). Furthermore, Eq. (3d) indicates that the terms in the left-hand side and that within the parentheses can be fairly neglected. Therefore, the set of governing equations [see Eqs. (1a)–(1d)], having considered the weak curvature approximation, can be rewritten as

$$\frac{\partial u_r}{\partial r} + \frac{u_r}{r} + \frac{1}{r} \frac{\partial u_\theta}{\partial \theta} + \frac{\partial u_z}{\partial z} = 0, \quad (4a)$$

$$-\frac{u_\theta^2}{r} = f_r - \frac{1}{\rho} \frac{\partial p}{\partial r} + \nu \frac{\partial^2 u_r}{\partial z^2}, \quad (4b)$$

$$\frac{\partial u_\theta}{\partial t} + u_r \frac{\partial u_\theta}{\partial r} + \frac{u_\theta}{r} \frac{\partial u_\theta}{\partial \theta} + u_z \frac{\partial u_\theta}{\partial z} + \frac{u_\theta u_r}{r} = f_\theta - \frac{1}{\rho r} \frac{\partial p}{\partial \theta} + \nu \frac{\partial^2 u_\theta}{\partial z^2}, \quad (4c)$$

$$f_z - \frac{1}{\rho} \frac{\partial p}{\partial z} = 0. \quad (4d)$$

For a turbulent flow, the set of governing equations of fluid dynamics [see Eqs. (1a)–(1d)] can be time averaged by employing the Reynolds decomposition for a turbulent flow.⁶ In doing so, we note that the gradients of the Reynolds shear stresses surpass those of the Reynolds normal stresses.¹¹ In addition, integrating Eq. (4d), the vertical momentum balance is expected to be primarily governed by the hydrostatic pressure intensity as $\rho^{-1} \partial p / \partial z = f_z = -g$, where g is the gravitational acceleration. Therefore, under a steady flow condition and setting $f_r = f_\theta = 0$, the set of governing equations under the weak curvature approximation [see Eqs. (4a)–(4d)] finally reduces to the Reynolds-averaged Navier–Stokes (RANS) equations. For brevity, keeping the symbols for the time-averaged quantities identical as in Eq. (1), the set of equations reduces to

$$\frac{\partial u_r}{\partial r} + \frac{u_r}{r} + \frac{\partial u_\theta}{\partial s} + \frac{\partial u_z}{\partial z} = 0, \quad (5a)$$

$$-\frac{u_\theta^2}{r} = -g S_r + \frac{1}{\rho} \frac{\partial \tau_{rz}}{\partial z}, \quad (5b)$$

$$u_r \frac{\partial u_\theta}{\partial r} + u_\theta \frac{\partial u_\theta}{\partial s} + u_z \frac{\partial u_\theta}{\partial z} + \frac{u_\theta u_r}{r} = g S_\theta + \frac{1}{\rho} \frac{\partial \tau_{\theta z}}{\partial z}, \quad (5c)$$

where (S_r, S_θ) and $(\tau_{rz}, \tau_{\theta z})$ are the radial and azimuthal components of the free surface slope and the total fluid shear stress, respectively. Note that the total fluid shear stress (henceforth called the shear stress, for brevity) comprises of the Reynolds shear stress and the viscous shear stress. Importantly, in the above formulation, the vertical momentum balance driven by the hydrostatic pressure intensity makes it possible to reduce the momentum equations to two dimensions.

The boundary conditions associated with the above set of equations are as follows:

- (i) No-slip at the bed and the sidewalls:

$$u_r = u_\theta = u_z = 0 \text{ at } z = z_b \text{ and } r = r_c \pm b, \quad (6a)$$

- (ii) Vanishing radial flux condition:

$$\int_{z_b}^{z_b+h} u_r dz = 0. \quad (6b)$$

However, the set of equations [see Eqs. (5a)–(5c)] falls short to close the system. Hence, appropriate turbulence closure

relationships, embodying reasonable approximations based on the physical ground, are sought to close the system.

B. Modeling strategies and constitutive formulations

The azimuthal shear stress can be modeled by applying the Boussinesq hypothesis, which expresses the fluid shear stress per unit mass density as a linear function of the local fluid strain rate via the turbulent diffusivity. It follows: $\tau_{\theta z} = \rho \varepsilon_{\theta z} (\partial u_{\theta} / \partial z + r^{-1} \partial u_z / \partial \theta) \approx \rho \varepsilon_{\theta z} \partial u_{\theta} / \partial z$, as evident from the weak curvature approximation. In a straight channel flow ($r_c \rightarrow \infty$), $\tau_{\theta z}$ takes the form of $\tau_{\theta z} = \tau_{0w} (1 - Z)$, where τ_{0w} is the bed shear stress ($\approx \rho g h S_{\theta}$), having considered the bed slope to be approximately equal to the free surface slope and Z is the scaled coordinate in the vertical direction $[(z - z_b) / h]$. However, the azimuthal bed shear stress $\tau_{0\theta}$ in a curved channel is smaller than the forward bed shear stress τ_{0w} in a straight channel owing to the redistribution of the primary flow momentum in the radial direction, triggered by the effects of curvilinear streamlines. To address the feedback between the primary flow and secondary current momentum, it suffices here to take $\tau_{0\theta} = \tau_{0w} (1 - \mathcal{L})$, where \mathcal{L} is the damping function that accounts for the reduction in primary flow momentum. The determination of \mathcal{L} is given in Sec. II E. It suggests that the azimuthal shear stress can be expressed as $\tau_{\theta z} = \rho g h S_{\theta} (1 - \mathcal{L}) (1 - Z)$. Therefore, $\varepsilon_{\theta z}$ is

$$\varepsilon_{\theta z} = g h^2 S_{\theta} (1 - \mathcal{L}) (1 - Z) \left(\frac{\partial u_{\theta}}{\partial Z} \right)^{-1}. \quad (7)$$

To evaluate the radial shear stress τ_{rz} , an isotropic notion of turbulent diffusivity is considered, implying $\tau_{rz} = \rho \varepsilon_{\theta z} (\partial u_r / \partial z + \partial u_z / \partial r) \approx \rho \varepsilon_{\theta z} \partial u_r / \partial z$, as evident from the weak curvature approximation. It is worth noting that in several numerical models based on RANS equations, for instance, the standard $k-\varepsilon$ model, the turbulent diffusivity is fundamentally considered to be isotropic. However, the primary drawback of such numerical models is that they are unable to capture the weak counter-rotating secondary cell, which is often found near the outer sidewall.³¹ The existence of this secondary cell was evidenced experimentally,^{20,25} and its precise origin was explained by the flow instability and the transfer of turbulent kinetic energy between the mean flow and turbulence. However, in this study, such a weak counter-rotating secondary cell near the outer wall is not considered. Therefore, using Eq. (7), τ_{rz} is expressed as

$$\tau_{rz} = \rho g h S_{\theta} (1 - \mathcal{L}) (1 - Z) \frac{\partial u_r}{\partial Z} \left(\frac{\partial u_{\theta}}{\partial Z} \right)^{-1}. \quad (8)$$

To find $\varepsilon_{\theta z}$ from Eq. (7), an exact expression for the azimuthal velocity u_{θ} is an essential prerequisite. On the other hand, Eq. (8) hinders to obtain an expression for the radial shear stress τ_{rz} because the radial velocity u_r is an unknown. It demands an additional formulation as a closure. To this end, we note that in Eq. (5b), the total acceleration component Du_r / Dt in the radial direction (that is the inertial terms) does not appear because of its minimal contribution, as was identified in the order of magnitude analysis. It is pertinent to discuss herein that Rozovskii¹¹ applied the method of consecutive approximations to find the error generated owing to ignoring the inertial terms. It was revealed that the effects of the inertial terms on the radial momentum balance are trivial as long as the channel is

weakly curved, specifically when the $\langle h \rangle / r_c$ ratio is less than 0.05. In fact, Eq. (5b) can be rearranged as $u_{\theta}^2 / r - g S_r = -\rho^{-1} \partial \tau_{rz} / \partial z$, which heralds the fact that the imbalance between the centrifugal force and the radial force is primarily driven by the vertical gradient of the radial shear stress. Integrating this relationship over the entire flow depth yields

$$g S_r + \frac{\tau_{0r}}{\rho h} - \int_0^1 \frac{u_{\theta}^2}{r} dZ = 0, \quad (9)$$

where τ_{0r} is the radial bed shear stress. Even the above simplified relationship remains unsolvable because the radial free surface slope S_r is still an unknown. As a first approximation, the contribution from the radial bed shear stress τ_{0r} to the radial momentum balance can be neglected by considering the third term of the left-hand side of Eq. (9) to be quite larger than the second term. From the physical rationale, this approximation is fairly reasonable because the radial free surface slope is principally overseen by the centrifugal acceleration. However, from the mathematical perspective, this approximation may be quasi-idealistic because the actual order of magnitude of the radial bed shear stress is not still in hand. To resolve this issue, Eq. (9) is modified as

$$S_r = \mathcal{J} \int_0^1 \frac{u_{\theta}^2}{g r} dZ, \quad (10)$$

where \mathcal{J} is the radial slope correction factor that can be obtained from the appropriate boundary condition. The determination of \mathcal{J} is given in Sec. II D. Equation (10) discloses that the radial slope correction factor effectively addresses the presence of radial shear stress into the mechanism of secondary circulation. From the physical rationale, the introduction of the radial slope correction factor can be further explained. In Eq. (10), the streamline curvature is approximated to be identical over the entire flow depth. However, in reality, the vertical fluid column possesses a differential streamline curvature due to the secondary circulation. The trajectory of the surface streamlines traces a larger radius, while that of the near-bed streamlines displays a smaller radius than the average radius of curvature. Besides, in the computation of centrifugal acceleration, the azimuthal velocity was solely considered rather than the total velocity because the azimuthal velocity remains the predominant velocity component, being largely sensitive to the effects of curvilinear streamlines. These key aspects need to be incorporated into the system while calculating the radial slope. Therefore, the inclusion of the radial slope correction factor in Eq. (10) is a requirement to address these issues. Equation (10) clearly demonstrates that at a given flow cross section, a radial inclination of the free surface is inevitable. An analytical expression for the radial free surface profile is developed in Sec. II C.

For a fully developed flow, the azimuthal velocity u_{θ} is independent of the azimuthal distance s , respecting the necessary boundary conditions as given in Eq. (6a). Furthermore, owing to the radial skew of the azimuthal velocity toward the outer sidewall, the location of the maximum azimuthal velocity, for a given vertical distance, is marginally away from the channel centerline. The azimuthal velocity can therefore be set as

$$u_{\theta} = \frac{\lambda + 1}{\lambda} U(r) Z^{1/\lambda} \text{ and } U(r) = U_c (1 - Y^2)^l \exp(l_2 Y), \quad (11)$$

where λ is the reciprocal of the power-law exponent, $U(r)$ is the depth-averaged azimuthal velocity at a given radial distance r , U_c is $U(r = r_c)$, Y is the scaled coordinate in the radial direction $(r - r_c)/b$, and l_1 and l_2 are the phenomenological constants. To be specific, l_1 signifies the qualitative radial growth of the sidewall boundary layers and l_2 defines the enrichment of the depth-averaged azimuthal velocity, in the zone away from the channel centerline, having a definite skewness in the azimuthal velocity profile. Clearly, in a straight channel flow, $l_2 = 0$, indicating a nonskewed azimuthal velocity profile. In Eq. (11), the azimuthal velocity scaled by its depth-averaged value obeys the power-law, which acts as a surrogate for the classical logarithmic law of the wall.³⁷ The existence of the power-law is well documented experimentally.^{11,22} The precise value of the reciprocal of the power-law exponent strongly depends on the Darcy–Weisbach friction factor. On the other hand, in Eq. (11), the depth-averaged azimuthal velocity scaled by the depth-averaged centerline azimuthal velocity follows a quadratic-cum-exponential law, whose legitimacy was also tested through experimental measurements.²² The validation of the abovementioned velocity laws with the experimental data is elaborated in Sec. III A. With Eq. (11), the area-averaged velocity, denoted by $\langle U \rangle$, is expressed as

$$\langle U \rangle = \frac{1}{A} \iint_A u_\theta dA = \frac{1}{A} \int_{Y=-1}^{Y=1} \int_{Z=0}^{Z=1} (u_\theta b h) dZ dY = \Psi U_c, \quad (12)$$

where A is the flow cross-sectional area and Ψ is a coefficient. They are expressed as

$$A = \int_{-1}^1 b h dY = 2b \langle h \rangle \quad \text{and} \quad \Psi = \frac{1}{2} \int_{-1}^1 (1 - Y^2)^{l_1} \exp(l_2 Y) dY. \quad (13)$$

Note that while performing the integration in Eq. (12), the differential dz is approximately taken as $dz = \langle h \rangle dZ$, keeping the flow depth $\langle h \rangle$ constant as an average value. However, the exact expression for the radial free surface profile is given in Sec. II C.

C. Radial free surface profile

Inserting Eq. (11) into Eq. (10) yields

$$S_r = \mathcal{J} \frac{(\lambda + 1)^2}{\lambda(\lambda + 2)} \frac{U_c^2}{g r} (1 - Y^2)^{2l_1} \exp(2l_2 Y). \quad (14)$$

The radial slope S_r can also be obtained from the relationship $S_r = dz_s/dr$. Since $z_s = z_b + h$ and $dz_b/dr = 0$ owing to the rigid bed condition (Fig. 1), it results in $S_r = dh/dr$. Substituting Eq. (14) into this relationship and integrating the resultant expression produces

$$h = h_c + \mathcal{J} \mathcal{C} \frac{(\lambda + 1)^2}{\lambda(\lambda + 2)} \frac{U_c^2}{g} \int_0^Y \frac{(1 - Y^2)^{2l_1} \exp(2l_2 Y)}{(1 + \mathcal{C}Y)} dY. \quad (15)$$

The above expression allows a direct estimation of the flow depth at a given radial distance. Then, the average flow depth $\langle h \rangle$ can be determined by averaging Eq. (15) over the flow cross section. The nondimensional flow depth $\hat{h} (=h/\langle h \rangle)$, after some algebra, takes the form as

$$\hat{h} = 1 + \frac{\mathcal{J}}{\Psi^2} \mathcal{C} \mathcal{F}^2 \frac{(\lambda + 1)^2}{\lambda(\lambda + 2)} \left[\int_0^Y \frac{(1 - Y^2)^{2l_1} \exp(2l_2 Y)}{(1 + \mathcal{C}Y)} dY - \frac{1}{2} \int_{-1}^1 \int_0^Y \frac{(1 - Y^2)^{2l_1} \exp(2l_2 Y)}{(1 + \mathcal{C}Y)} dY dY \right], \quad (16)$$

where \mathcal{F} is the flow Froude number $[= \langle U \rangle / (g \langle h \rangle)^{0.5}]$.

D. Determination of radial slope correction factor

Since the expression for the radial slope S_r is known [see Eq. (14)], the radial shear stress τ_{rz} can therefore be obtained from the following radial momentum balance [see Eq. (5b)]: $\rho^{-1} \partial \tau_{rz} / \partial z = g S_r - u_\theta^2 / r$. τ_{rz} must vanish at the free surface, implying $\tau_{rz}(Z = 1) = 0$. Substituting the expressions for u_θ and S_r from Eqs. (11) and (14), respectively, into the radial momentum balance and then integrating the resulting expression yield

$$\tau_{rz} = \rho U^2 \frac{h}{r} \frac{(\lambda + 1)^2}{\lambda(\lambda + 2)} \left[\mathcal{J}(Z - 1) - (Z^{(2+\lambda)/\lambda} - 1) \right]. \quad (17)$$

Substituting the above relationship into Eq. (8) and using Eq. (11), the vertical gradient of the radial velocity $\partial u_r / \partial Z$ is obtained. Subsequently, the resulting expression is integrated, using Eq. (6a), to derive the expression for the radial velocity u_r as

$$u_r = G \left[\mathcal{J} \lambda Z^{1/\lambda} + \frac{\lambda}{\lambda + 3} Z^{(3+\lambda)/\lambda} {}_2F_1 \left(1, \frac{3}{\lambda} + 1; 2 + \frac{3}{\lambda}; Z \right) - \lambda Z^{1/\lambda} {}_2F_1 \left(1, \frac{1}{\lambda}; 1 + \frac{1}{\lambda}; Z \right) \right], \quad (18a)$$

$$G = - \frac{(\lambda + 1)^3}{\lambda^3 (\lambda + 2)} \frac{U^3}{g r (1 - \mathcal{L}) S_\theta}. \quad (18b)$$

u_r also satisfies the vanishing radial flux condition, as given in Eq. (6b). Inserting Eq. (18) into Eq. (6b) results in

$$\mathcal{J} = - \frac{\lambda + 1}{\lambda^2} \left[\frac{\lambda^2}{(\lambda + 3)(2\lambda + 3)} {}_2F_1 \left(1, 1 + \frac{3}{\lambda}; 3 + \frac{3}{\lambda}; 1 \right) - \frac{\lambda^2}{\lambda + 1} {}_2F_1 \left(1, \frac{1}{\lambda}; 2 + \frac{1}{\lambda}; 1 \right) \right], \quad (19)$$

where ${}_2F_1$ is the special type of the generalized hypergeometric function ${}_pF_q(a_1, \dots, a_p; b_1, \dots, b_q; x)$. The variation of the radial slope correction factor \mathcal{J} with reciprocal of the power-law exponent λ is depicted in Fig. 2. It is apparent that \mathcal{J} weakly dampens with an increase in λ . Recalling the preformulated relationships [Eqs. (9) and (10)], we find that the contribution from the radial bed shear stress per unit mass density and local flow depth to the radial momentum balance, for $\lambda \in [5, 15]$, is 0.8%–5% of the dominated depth-averaged curvature induced term $\int (u_\theta^2 / r) dr dZ$. Although this estimation is in no way colossal, the inclusion of the radial slope correction factor is a key stride toward the physical understanding of the radial momentum balance (see Sec. II B).

E. Determination of damping function

The vertical velocity u_z is determined by integrating the continuity equation [Eq. (5a)] and obeying the no-slip at the channel

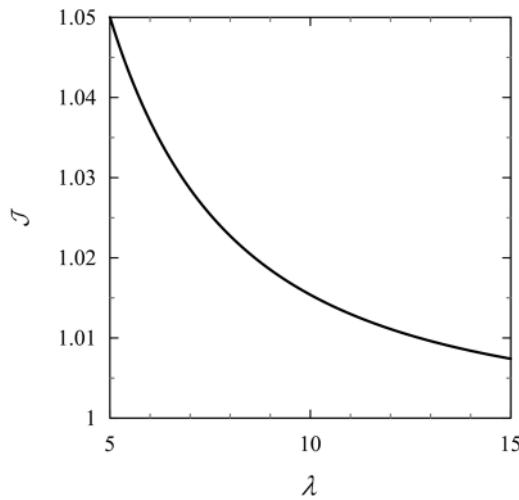


FIG. 2. Dependency of the radial slope correction factor \mathcal{J} on reciprocal of the power-law exponent λ .

boundary [Eq. (6a)]. To perform the integration, the transformations $\partial Z/\partial r = -h^{-1}Z\partial h/\partial r$ and $\partial Z/\partial s = h^{-1}S_\theta$ are applied. Finally, u_z takes the following form:

$$u_z = -\left[\frac{dh}{dr} + h\left(\frac{3}{U}\frac{dU}{dr} + \frac{1}{1-\mathcal{L}}\frac{d\mathcal{L}}{dr}\right)\right] \int_0^Z u_r dZ + u_r Z \frac{dh}{dr} - u_\theta S_\theta. \quad (20)$$

Since the three-dimensional velocity components are known [see Eqs. (11), (18), and (20)], the azimuthal shear stress $\tau_{\theta z}$ can be determined by performing the momentum integral of Eq. (5c). In doing so and applying the boundary condition $\tau_{\theta z}(Z = 1) = 0$, $\tau_{\theta z}$ reads

$$\tau_{\theta z} = \rho h(I_1 + I_2 + I_3 + I_4 + I_5), \quad (21)$$

where the expressions for I_{1-5} are given by

$$I_1 = (1 - Z)gS_\theta, \quad (22a)$$

$$I_2 = \frac{\partial}{\partial s} \int_1^Z u_\theta^2 dZ = \frac{S_\theta}{h} U^2 \left(\frac{\lambda + 1}{\lambda}\right)^2 (Z^{2/\lambda} - 1), \quad (22b)$$

$$I_3 = \frac{\partial}{\partial r} \int_1^Z u_\theta u_r dZ = \frac{\lambda + 1}{\lambda} \left[U \left(u_r Z^{1/\lambda} \frac{\partial Z}{\partial r} - u_r \Big|_{Z=1} \frac{\partial Z}{\partial r} \Big|_{Z=1} \right) + \frac{1}{G} \frac{\partial}{\partial r} (GU) \int_1^Z u_r Z^{1/\lambda} dZ \right], \quad (22c)$$

$$I_4 = \left(\frac{2}{r} + \frac{1}{h} \frac{dh}{dr} \right) \int_1^Z u_\theta u_r dZ = \frac{\lambda + 1}{\lambda} U \left(\frac{2}{r} + \frac{1}{h} \frac{dh}{dr} \right) \int_1^Z u_r Z^{1/\lambda} dZ, \quad (22d)$$

$$I_5 = u_\theta u_z \Big|_Z - (u_\theta u_z) \Big|_{Z=1}. \quad (22e)$$

In the above expressions, the term I_1 represents the linear profile of azimuthal shear stress, occurring in a straight channel flow having a zero-pressure gradient. The term I_2 signifies the change in the advective transport of azimuthal momentum, while the term I_3 characterizes the change in the redistribution of the azimuthal momentum in the radial direction due to the curvilinear deflection of the primary flow. On the other hand, the terms I_4 and I_5 demonstrate the complex correlations of the secondary current velocity components in the momentum balance with the azimuthal velocity. Using the above set of expressions [Eqs. (22a)–(22e)] and the relationship $r^{-1} + G^{-1}\partial G/\partial r = 3U^{-1}\partial U/\partial r + (1 - \mathcal{L})^{-1}\partial \mathcal{L}/\partial r$ [from Eq. (18b)], Eq. (21) takes the following form:

$$\begin{aligned} \tau_{\theta z} = \rho h & \left[(1 - Z)gS_\theta + \frac{\lambda + 1}{\lambda} \left(4 \frac{\partial U}{\partial r} + \frac{U}{r} + \frac{U}{1 - \mathcal{L}} \frac{\partial \mathcal{L}}{\partial r} + \frac{U}{h} \frac{\partial h}{\partial r} \right) \right. \\ & \times \int_1^Z u_r Z^{1/\lambda} dZ - \frac{\lambda + 1}{\lambda} Z^{1/\lambda} \left(3 \frac{\partial U}{\partial r} + \frac{U}{1 - \mathcal{L}} \frac{\partial \mathcal{L}}{\partial r} + \frac{U}{h} \frac{\partial h}{\partial r} \right) \\ & \left. \times \int_0^Z u_r dZ \right]. \quad (23) \end{aligned}$$

The azimuthal bed shear stress $\tau_{\theta\theta}$ can be obtained from Eq. (23) by extending the total bed shear stress to the bed, implying that $\tau_{\theta\theta} = \tau_{\theta z}(Z = 0)$. It produces

$$\tau_{\theta\theta} = \rho h \left[gS_\theta - \frac{\lambda + 1}{\lambda} \left(4 \frac{\partial U}{\partial r} + \frac{U}{r} + \frac{U}{1 - \mathcal{L}} \frac{\partial \mathcal{L}}{\partial r} + \frac{U}{h} \frac{\partial h}{\partial r} \right) GI_6 \right], \quad (24a)$$

$$\begin{aligned} I_6 = \mathcal{J} \frac{\lambda^2}{\lambda + 2} {}_3F_2 \left(1, 1 + \frac{3}{\lambda}, 2 + \frac{4}{\lambda}; 2 + \frac{3}{\lambda}, 3 + \frac{4}{\lambda}; 1 \right) \\ - \frac{\lambda^2}{\lambda + 2} {}_3F_2 \left(1, \frac{1}{\lambda}, 1 + \frac{2}{\lambda}; 1 + \frac{1}{\lambda}, 2 + \frac{2}{\lambda}; 1 \right). \quad (24b) \end{aligned}$$

$\tau_{\theta\theta}$ can also be obtained from $\tau_{\theta\theta} = \rho ghS_\theta(1 - \mathcal{L})$. Averaging this relationship over the flow cross section gives the area-averaged azimuthal bed shear stress as $\langle \tau_{\theta\theta} \rangle = \rho g \langle h \rangle S_\theta (1 - \langle \mathcal{L} \rangle)$. $\langle \tau_{\theta\theta} \rangle$ can be found from the well-known friction factor conjecture, which reads $\langle \tau_{\theta\theta} \rangle = (f/8)\rho \langle U \rangle^2$, where f is the Darcy–Weisbach friction factor. This constitutive formulation yields $g \langle h \rangle S_\theta (1 - \langle \mathcal{L} \rangle) = (f/8)\langle U \rangle^2$. The f can be estimated from $f = 8\kappa^2 \lambda^{-2}$, where κ is the von Kármán constant (≈ 0.41). This relationship is supported by a large corpus of experimental data in curved channels.²³ Equating Eq. (24a) with the relationship $\tau_{\theta\theta} = \rho ghS_\theta(1 - \mathcal{L})$ and keeping in mind the constitutive equation, the resultant expression produces an ordinary differential equation of the damping function \mathcal{L} . This differential equation hinders to attain a complete solution of \mathcal{L} as a function of radial distance because a precise boundary condition for the damping function invites another intricacy into the formulation. To get rid of this inherent complexity, the differential equation is averaged over the flow cross section to obtain an area-averaged value of \mathcal{L} . Thus, the area-averaged damping function $\langle \mathcal{L} \rangle$ reads

$$\langle \mathcal{L} \rangle = \left[1 - \frac{\lambda^4(\lambda + 2)\Psi^4 f^2 \mathcal{A}^2}{32(\lambda + 1)^4 I_6 \mathcal{C}^2 I_7} \right]^{-1}, \quad (25a)$$

$$I_7 = \int_{-1}^1 \frac{(1 - Y^2)^{4l_1} \exp(4l_2 Y)}{1 + CY} \times \left[\frac{4}{\tilde{C}} \left(l_2 - \frac{2l_1 Y}{1 - Y^2} \right) + \frac{1}{1 + CY} + \mathcal{J} \frac{(\lambda + 1)^2}{\lambda(\lambda + 2)} \mathcal{F}^2 \right] dY. \quad (25b)$$

F. Flow circulation about azimuthal axis and flow helicity

The strength of a rotational flow field is quantified by the circulation, which provides a measure of the vorticity flux. The circulation can be obtained from the integral of the vorticity over a closed superficial frame. Here, we primarily focus on the azimuthal vorticity Ω_θ ($=\partial u_z/\partial r - \partial u_r/\partial z$), owing to its close link with the secondary circulation on the radial plane (rz -plane). Considering an appropriate time scale as $\langle T \rangle = \langle h \rangle / \langle U \rangle$, Ω_θ in a nondimensional form, denoted by $\hat{\Omega}_\theta = \Omega_\theta \langle T \rangle$, is expressed as

$$\hat{\Omega}_\theta = \frac{1}{\mathcal{A}} \frac{\partial \hat{u}_z}{\partial Y} - \frac{1}{\hat{h}} \frac{\partial \hat{u}_r}{\partial Z}, \quad (26)$$

where the nondimensional velocity components are expressed as $(\hat{u}_r, \hat{u}_\theta, \hat{u}_z) = (u_r, u_\theta, u_z) / \langle U \rangle$.

The flow circulation Γ_θ about the azimuthal axis reads

$$\Gamma_\theta = \iint_{r,z} \Omega_\theta dr dz. \quad (27)$$

Using Eq. (26), Γ_θ in a nondimensional form, denoted by $\hat{\Gamma}_\theta = \Gamma_\theta (b \langle U \rangle)^{-1}$, is expressed as

$$\hat{\Gamma}_\theta = \int_{Y=-1}^1 \int_{Z=0}^1 \left(\frac{1}{\mathcal{A}} \frac{\partial \hat{u}_z}{\partial Y} - \frac{1}{\hat{h}} \frac{\partial \hat{u}_r}{\partial Z} \right) dZ dY. \quad (28)$$

The helicity of a fluid flow is topologically understood as a measure of knottedness of vortex lines.³⁸ If \mathbf{u} and $\nabla \times \mathbf{u}$ denote the velocity field and the vorticity field, respectively, then the helicity contained in volume V , bounded by a closed superficial frame, is expressed as

$$H = \iiint_V \mathbf{u} \cdot (\nabla \times \mathbf{u}) dV. \quad (29)$$

The components of ∇ in the cylindrical polar coordinate system are written as $\nabla = (\partial/\partial r, r^{-1}\partial/\partial\theta, \partial/\partial z)$. H is a quasiscalar quantity, which is apt to be a measure of flow chirality, because it changes sign under an appropriate choice of frame of reference. Equation (29) can be explicitly expressed in three dimensions as

$$H = \iiint_V \left[u_\theta \left(\frac{\partial u_z}{\partial r} - \frac{\partial u_r}{\partial z} \right) + u_r \left(\frac{\partial u_\theta}{\partial z} - \frac{\partial u_z}{\partial s} \right) + u_z \left(\frac{\partial u_r}{\partial s} - \frac{\partial u_\theta}{\partial r} \right) \right] ds dr dz. \quad (30)$$

For a fully developed flow, the nondimensional form of helicity per unit azimuthal distance, denoted by $\hat{H} = H(b \langle U \rangle^2)^{-1}$, is expressed as

$$\hat{H} = \int_{Y=-1}^1 \int_{Z=0}^1 \left[\hat{u}_\theta \left(\frac{1}{\mathcal{A}} \frac{\partial \hat{u}_z}{\partial Y} - \frac{1}{\hat{h}} \frac{\partial \hat{u}_r}{\partial Z} \right) + \hat{u}_r \frac{1}{\hat{h}} \frac{\partial \hat{u}_\theta}{\partial Z} - \hat{u}_z \frac{1}{\mathcal{A}} \frac{\partial \hat{u}_\theta}{\partial Y} \right] dZ dY. \quad (31)$$

III. RESULTS AND DISCUSSION

A. Velocity field

The validation of the power-law of velocity profile, where the azimuthal velocity u_θ scaled by its depth-averaged value $U(r)$ obeys the power-law relationship in accordance with Eq. (11), is shown in Fig. 3. The experimental data for fully developed flow in a curved channel taken from de Vriend and Koch²² are used for the validation. In fact, two experimental runs are considered, corresponding to two different fluid fluxes as $Q = 0.232$ and $0.463 \text{ m}^3 \text{ s}^{-1}$. For each of the experimental runs, the velocity measurements at three distinct vertical sections 4, 8, and 11 are depicted in Figs. 3(a) and 3(b). These sections correspond to the nondimensional radial distance $Y = 0.45, -0.15, \text{ and } -0.6$, respectively. Depending on the values of the friction factor in these two experimental runs, the reciprocal of the power-law exponent λ , obtained from the friction factor conjecture, is 8 and 10, respectively. The theoretical velocity profiles offer a satisfactory congruence with the experimental data, suggesting the inevitable existence of the power-law. Note that the experimental

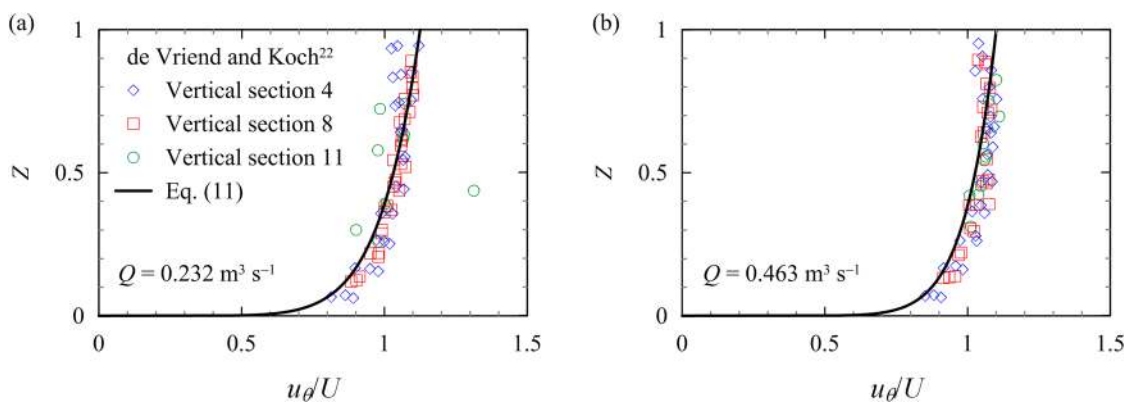


FIG. 3. Vertical profiles of nondimensional azimuthal velocity u_θ scaled by its depth-averaged value $U(r)$ and the experimental data for fluid fluxes Q of (a) $0.232 \text{ m}^3 \text{ s}^{-1}$ and (b) $0.463 \text{ m}^3 \text{ s}^{-1}$.

data close to the free surface ($Z = 1$), especially in Fig. 3(b), suggest a slight dip-phenomenon, predicting a negative strain rate at the extremity of the boundary layer. The dip-phenomenon cannot be fully captured by the power-law. However, such an aspect is of secondary importance here because the present formulation is devoid of any dip-phenomenon owing to the large ratio of channel width to average flow depth ($2A \geq 20$).

The depth-averaged azimuthal velocity $U(r)$ scaled by the depth-averaged centerline azimuthal velocity as a function of nondimensional radial distance Y is shown in Fig. 4. The experimental data of de Vriend and Koch²² for two different fluid fluxes, $Q = 0.232$ and $0.463 \text{ m}^3 \text{ s}^{-1}$, are also plotted. For a given fluid flux, the velocity data at different azimuthal sections, where the flow almost attains a fully developed state, are considered. These sections include C_0 , D_0 , D_1 , and E_0 in the experimental setup of de Vriend and Koch.²² The experimental data clearly predict an outward shift of the depth-averaged azimuthal velocity profile arising from the effects of curvilinear streamlines. The radial profile of U/U_c satisfactorily obeys the quadratic-cum-exponential law, as given in Eq. (11). The phenomenological constants l_1 and l_2 , corresponding to the experimental data, are obtained as 0.3 and 0.65, respectively. These values can be treated as approximately constant for different flow conditions as long as the channel is weakly curved, allowing a quasiuniversal velocity profile in a curved channel. In this context, it is worth noting that the theoretical azimuthal velocity profile does not consider any flow separation from the inner sidewall. For flow in a strongly curved channel ($b/r_c > 0.1$), the flow separation near the inner sidewall can hardly be avoided and the approximations involved in the boundary layer equations no longer apply. In Fig. 4, the experimental data close to the channel sidewalls ($Y \rightarrow \pm 1$) slightly depart from the quadratic-cum-exponential law. This may be attributed to the uncertainties that linger in the velocity measurements owing to the substantial three-dimensional effects close to the sidewalls.

Figure 5 shows the contours of nondimensional azimuthal velocity \hat{u}_θ (azimuthal velocity scaled by the area-averaged velocity), on a nondimensional YZ -plane bounded by $Y \in [-1, 1]$ and $Z \in [0, 1]$, for $\lambda = 7$. Quite evidently, the skewing of the velocity filament toward the outer sidewall governed by the quadratic-cum-exponential law

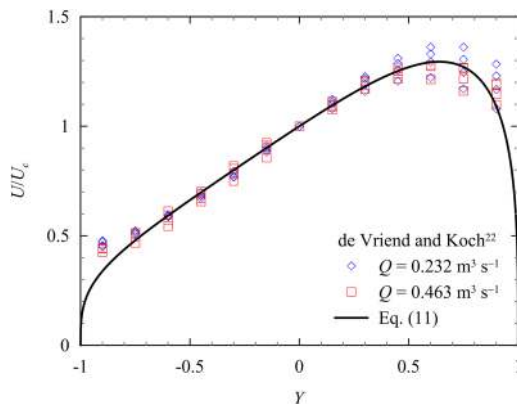


FIG. 4. Radial profile of nondimensional depth-averaged azimuthal velocity $U(r)$ scaled by the depth-averaged centerline azimuthal velocity U_c and the experimental data for different fluid fluxes.

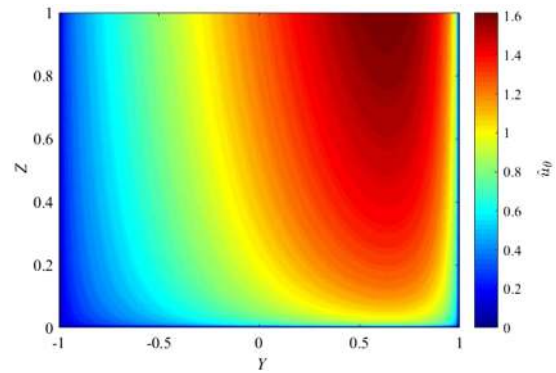


FIG. 5. Contours of nondimensional azimuthal velocity $\hat{u}_\theta (=u_\theta/\langle U \rangle)$ on nondimensional YZ -plane for reciprocal of the power-law exponent $\lambda = 7$.

in conjunction with the power-law controls the variability of the azimuthal velocity over the vertical and radial extents. At the channel centerline, the azimuthal velocity u_θ approximately becomes the area-averaged velocity $\langle U \rangle$ at 20% of the flow depth ($Z = 0.2$). On the other hand, away from the channel centerline ($Y > 0$), the location of $\hat{u}_\theta = 1$ shifts closer to the bed with an increase in the radial distance Y up to $Y = 0.7$ owing to the velocity enhancement resulting from the effects of curvilinear streamlines. However, beyond $Y = 0.7$, the azimuthal velocity dampens in the presence of the outer sidewall, where the velocity vanishes to preserve the no-slip. Therefore, the location of $\hat{u}_\theta = 1$ shifts toward the free surface for $Y > 0.7$. Note that the radial location Y_m of the maximum depth-averaged azimuthal velocity can be found from Eq. (11) by setting $dU/dY = 0$, resulting in $Y_m = (1 + l_r^2)^{1/2} - l_r$, where $l_r = l_1/l_2$. For $(l_1, l_2) = (0.3, 0.65)$, it yields $Y_m = 0.64$. This closely corresponds to the value of l_2 since l_2 provides a measure of the skewness in the azimuthal velocity profile. At $Y_m = 0.64$, the azimuthal velocity reaches almost 1.6 times the area-averaged velocity at the free surface. The spatial distributions of azimuthal velocity substantially affect the estimations of momentum and energy fluxes based on the area-averaged velocity. In order to elicit a quantitative understanding of these fluxes, it is required to find the Boussinesq and the Coriolis coefficients. Since the fluid flux in a curved channel is primarily driven by the azimuthal velocity, the Boussinesq and the Coriolis coefficients, denoted by β and α , respectively, are expressed as follows:⁶

$$\beta = \frac{1}{A\langle U \rangle^2} \iint_A u_\theta^2 dA = \frac{(\lambda + 1)^2}{2\Psi^2\lambda(\lambda + 2)} \int_{-1}^1 (1 - Y^2)^{2l_1} \exp(2l_2 Y) dY, \tag{32}$$

$$\alpha = \frac{1}{A\langle U \rangle^3} \iint_A u_\theta^3 dA = \frac{(\lambda + 1)^3}{2\Psi^3\lambda^2(\lambda + 3)} \int_{-1}^1 (1 - Y^2)^{3l_1} \exp(3l_2 Y) dY. \tag{33}$$

Ψ appearing in the above equations is computed from Eq. (13). For $\lambda = 7$, the Boussinesq and Coriolis coefficients are $\beta = 1.141$ and $\alpha = 1.408$, respectively. In a straight channel flow, β and α approximately vary in the range 1.01–1.12 and 1.03–1.36, respectively.⁶ It suggests that in a curved channel flow, the Boussinesq and Coriolis

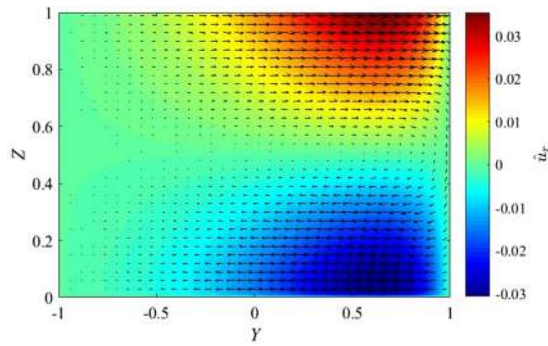


FIG. 6. Nondimensional velocity vectors on a nondimensional YZ-plane superimposed on the contours of nondimensional radial velocity $\hat{u}_r (=u_r/\langle U \rangle)$ for curvature ratio $C (=b/r_c) = 0.04$, reciprocal of the power-law exponent $\lambda = 7$, and aspect ratio $\mathcal{A} (=b/\langle h \rangle) = 20$.

coefficients slightly exceed their corresponding upper limits in a straight channel flow.

Figure 6 depicts the contours of nondimensional radial velocity \hat{u}_r (radial velocity scaled by the area-averaged velocity), on a nondimensional YZ-plane. In addition, the nondimensional velocity vectors, having magnitude $(\hat{u}_r^2 + \hat{u}_z^2)^{1/2}$ and direction $\tan^{-1}(\hat{u}_z/\hat{u}_r)$, are illustrated. The velocity vectors clearly manifest a clockwise circulatory fluid motion in the YZ-plane. The contours show that the radial velocity changes its sign at $Z \approx 0.5$, where it is quite feeble and thus practically negligible. However, the intensity of the radial velocity is relatively strong near the bed and the free surface at radial distance $Y \approx 0.65$. This location closely corresponds to the position of the maximum depth-averaged azimuthal velocity (Fig. 4). However, close to the outer sidewall, the radial velocity weakens to preserve the no-slip. At a given vertical distance, the absolute magnitudes of the velocity vectors, in the zone away from the sidewalls, gradually increase toward the outer sidewall. Away from the sidewalls, the velocity vectors are approximately parallel to the bed since the magnitude of the vertical velocity is trivial there as compared to the radial velocity. However, close to the sidewalls, the velocity vectors are rather skewed due to the sizeable amount of the vertical velocity.

A fundamental question, in this instance, arises: how is the radial velocity sensitive to a set of key parameters? To answer this question, the important parameters are considered to be the curvature ratio C , the reciprocal of the power-law exponent λ , and the aspect ratio \mathcal{A} . To be specific, the reciprocal of the power-law exponent λ is closely related to the Darcy–Weisbach friction factor f as $\lambda \propto 1/f^{0.5}$ (see Sec. II E). Therefore, the variations in the reciprocal of the power-law exponent essentially reflect the corresponding changes in the resistance to flow. Since the velocity components are made nondimensional by the area-averaged velocity in the numerical experiment, it was found that the effects of the flow Froude number on the vertical profiles of radial velocity no longer exist. However, to evaluate any parameters that weakly depend on the flow Froude number, $\mathcal{F} = 0.3$ is considered. The vertical profiles of \hat{u}_r , at the channel centerline ($Y = 0$) for different values of C , λ , and \mathcal{A} are furnished in Figs. 7(a)–7(c). Importantly, when a specific parameter is varied, the remaining two parameters are kept as constant.

The constant set of parameters in Figs. 7(a)–7(c) is considered as $(C, \lambda, \mathcal{A}) = (0.04, 7, 20)$. Figures 7(a)–7(c) show that for a given C , λ , and \mathcal{A} , the radial velocity sharply diminishes (increase in negative magnitude) with a small increase in the vertical distance, forming a protuberance to attain a maximum negative peak. Then, the radial velocity increases (reduction in negative magnitude) with the vertical distance, becoming zero roughly at the mid-flow depth ($Z = 0.5$). Above $Z = 0.5$, the radial velocity becomes positive and increases as one moves toward the free surface. With an increase in the curvature ratio, the absolute magnitude of the radial velocity intensifies throughout the flow depth, as evident from Fig. 7(a). It is attributed to the fact that the centrifugal acceleration escalates with an increase in the curvature ratio as the former is inversely proportional to the radius of curvature. The radial velocity profiles for different curvature ratios clearly display a pivoting point, located at $Z \approx 0.5$, through which the profiles emerge [Fig. 7(a)]. This point closely corresponds to the occurrence of vanishing radial velocity. For a given vertical distance, especially for $Z < 0.1$, the radial velocity increases, as the reciprocal of the power-law exponent λ increases [Fig. 7(b)], whereas for $Z > 0.3$, the radial velocity profiles are practically independent of λ , suggesting that the profiles become frozen for $\lambda > 7$. Another important observation is that unlike Fig. 7(a), the pivoting point of the radial velocity profiles for different λ occurs at $Z \approx 0.33$. Importantly, the position of the vanishing radial velocity marginally shifts downward with an increase in λ . Figure 7(c) indicates that as the aspect ratio increases, the absolute magnitude of the radial velocity deteriorates over the entire flow depth. However, for a large aspect ratio ($\mathcal{A} > 30$), the radial velocity profiles attain a quasifrozen state. Akin to Fig. 7(a), the pivoting point in Fig. 7(c) is formed at $Z \approx 0.5$.

Figures 7(a)–7(c) do not provide an understanding of how the radial velocity, for a given vertical distance, is distributed in the radial direction. To gain a quantitative insight of this scenario, the radial profiles of radial velocity are shown in Fig. 7(d), for two different nondimensional vertical distances $Z = 0.4$ and 0.6 , where the radial velocity is directed toward inner and outer sidewalls, respectively. Noticeably, the radial velocity, for a given vertical distance, becomes stronger (in the absolute sense) near the outer sidewall, attaining its peak at $Y \approx 0.65$, and thereafter abruptly reduces toward the outer sidewall.

Figures 8(a) and 8(b) provide an experimental verification of the radial velocity obtained from the theoretical analysis. The experimental data of radial velocity at two vertical sections, located at $Y = -0.15$ and 0.45 , are taken from de Vriend and Koch²² for two different fluid fluxes. In general, the comparisons of the theoretical profiles with the experimental data are satisfactory. Note that in the near-bed flow zone, the radial velocity sharply dampens to preserve the no-slip [see Eq. (6a)]. However, the experimental data of de Vriend and Koch²² could not capture the velocity slowdown in the near-bed flow zone and the no-slip owing to the limitation of the experiment.

Figure 9 shows the contours of nondimensional azimuthal vorticity $\hat{\Omega}_\theta$, in the near-bed flow zone, on the nondimensional YZ-plane bounded by $Y \in [-1, 1]$ and $Z \in [0, 0.1]$, for $C = 0.04$, $\lambda = 7$, and $\mathcal{A} = 20$. It is evident that in the immediate vicinity of the bed, the flow possesses a large azimuthal vorticity resulting from a steep velocity gradient. Importantly, the azimuthal vorticity, in the close proximity of the bed, is greater toward the outer sidewall than toward the

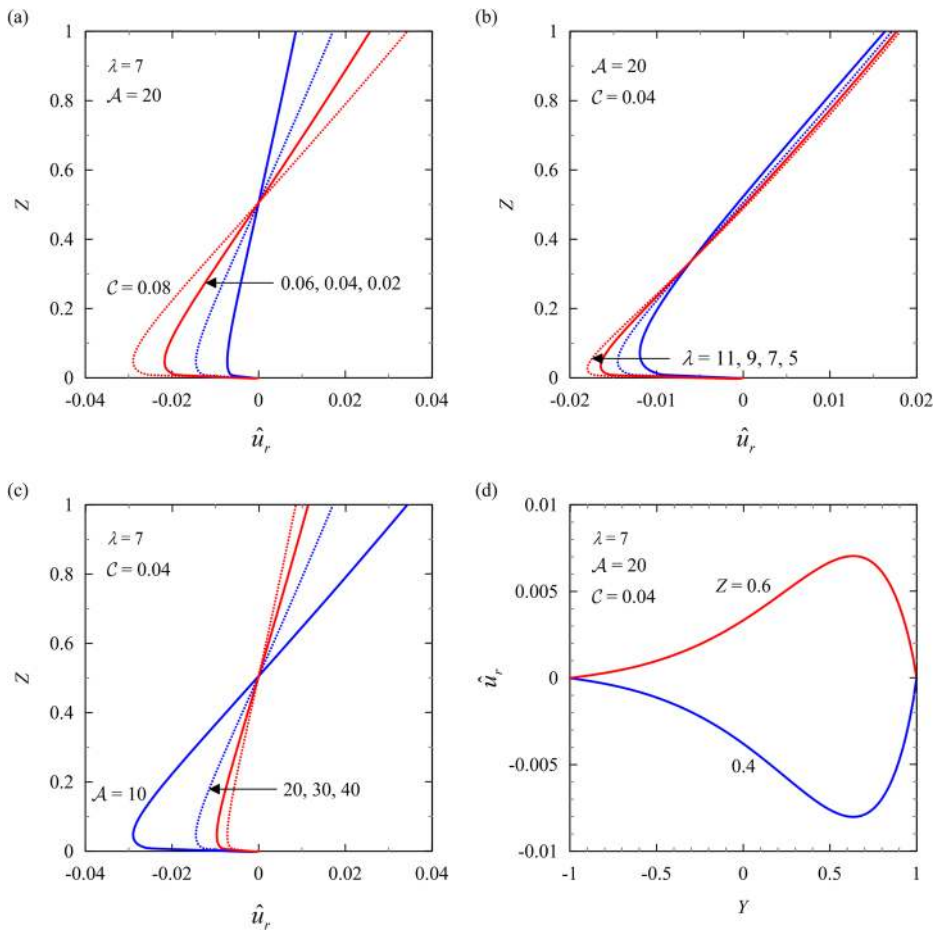


FIG. 7. Vertical profiles of nondimensional radial velocity $\hat{u}_r (=u_r/\langle U \rangle)$ at the channel centerline for (a) curvature ratios $C (=b/r_c) = 0.02, 0.04, 0.06,$ and $0.08,$ (b) reciprocal of the power-law exponents $\lambda = 5, 7, 9,$ and $11,$ and (c) aspect ratios $\mathcal{A} (=b/\langle h \rangle) = 10, 20, 30,$ and $40.$ (d) Radial profiles of nondimensional radial velocity \hat{u}_r at nondimensional vertical distances $Z = 0.4$ and $0.6.$

inner sidewall. However, the magnitude of the azimuthal vorticity abruptly diminishes as one moves toward the free surface.

Figures 10(a) and 10(b) represent the variations of nondimensional flow circulation $\hat{\Gamma}$ about azimuthal axis and flow helicity \hat{H}

per unit azimuthal distance with curvature ratio C and aspect ratio \mathcal{A} , respectively. In the numerical experiments, we revealed that the $\hat{\Gamma}$ and \hat{H} hardly vary with the reciprocal of the power-law exponent λ . Therefore, such weak dependencies of $\hat{\Gamma}$ and \hat{H} on λ are not

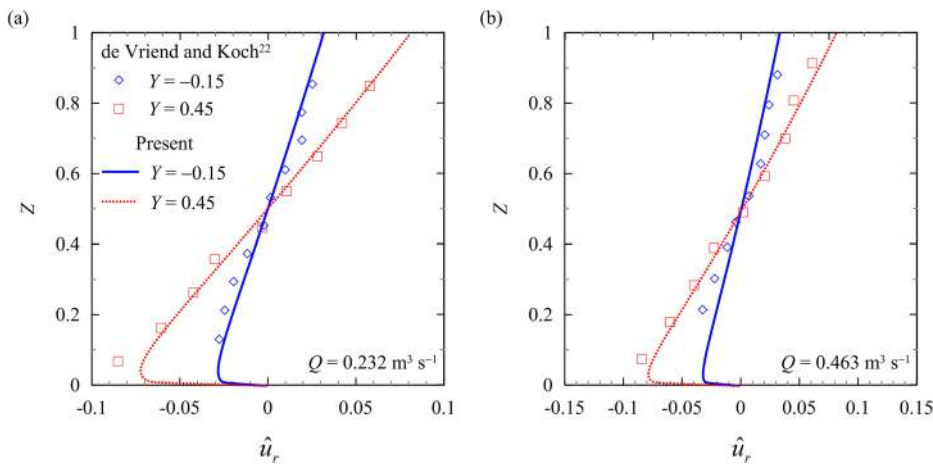


FIG. 8. Comparison of vertical profiles of nondimensional radial velocity $\hat{u}_r (=u_r/\langle U \rangle)$ with the experimental data for fluid fluxes Q of (a) $0.232 \text{ m}^3 \text{ s}^{-1}$ and (b) $0.463 \text{ m}^3 \text{ s}^{-1}.$

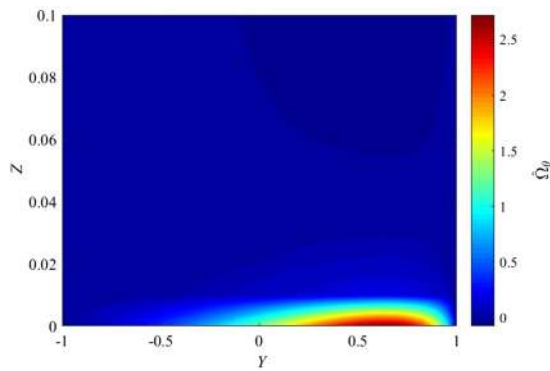


FIG. 9. Contours of nondimensional azimuthal vorticity $\hat{\Omega}_\theta (= \Omega_\theta \langle h \rangle / \langle U \rangle)$ on the nondimensional YZ-plane for the curvature ratio $C (= b/r_c) = 0.04$, reciprocal of the power-law exponent $\lambda = 7$, and aspect ratio $\mathcal{A} (= b/\langle h \rangle) = 20$.

furnished herein. In Fig. 10, both the nondimensional flow circulation about the azimuthal axis and flow helicity are negative since they are closely associated with the global sense of secondary circulation, being in the clockwise direction (see Fig. 6). In addition, the nondimensional flow circulation about the azimuthal axis and flow helicity strengthen (in the absolute sense) with an increase in the curvature ratio, while they decrease as the aspect ratio increases.

B. Radial free surface profile

The radial free surface profile for a set of key parameters can be obtained from Eq. (16). Equation (16) shows that the radial free surface profile is dependent on the appropriate selection of the flow Froude number \mathcal{F} , curvature ratio C , and slope correction factor \mathcal{J} , which is a function of the reciprocal of the power-law exponent λ [see Eq. (19)]. However, in the numerical experiment, we identified that the radial free surface profile is less sensitive to λ because \mathcal{J} is a weak function of λ . Therefore, the sensitivity of the radial free surface profile to λ is not presented here. Figures 11(a) and 11(b) show the radial free surface profiles for different flow Froude numbers \mathcal{F} and curvature ratios C . In Fig. 11(a), C is kept constant as 0.04, while in Fig. 11(b), \mathcal{F} is considered to be 0.3. For a given radial distance Y , near the inner sidewall, the free surface level reduces with

an increase in the flow Froude number [Fig. 11(a)], whereas near the outer sidewall, it rises with the flow Froude number. These features emerge from the predominant effects of centrifugal acceleration in a curved channel flow. Similar observations are also evident from Fig. 11(b). In essence, the radial free surface profiles evolve more quickly with the flow Froude number than with the curvature ratio since the radial free surface profile has a quadratic tie-up with the flow Froude number [see Eq. (16)]. Note that the average flow depth $\langle h \rangle$ over the flow cross section, that is $\hat{h} = 1$, is located slightly away from the channel centerline.

It is also interesting to examine the variations of superelevation with the flow Froude number and curvature ratio. The superelevation Δh can be readily obtained from the relationship $\Delta h = h(Y = 1) - h(Y = -1)$. The variations of nondimensional superelevation $\Delta \hat{h} (= \Delta h / \langle h \rangle)$ with the flow Froude number \mathcal{F} and curvature ratio C are presented in Figs. 11(c) and 11(d). It is revealed that the superelevation follows a nonlinear relationship with the flow Froude number, while it varies approximate linearly with the curvature ratio.

The experimental verifications of the radial free surface profiles, obtained from the theoretical analysis, are presented in Fig. 12. In Fig. 12(a), the theoretical variation of flow depth h scaled by the flow depth at the channel centerline h_c with the nondimensional radial distance Y is compared with the experimental data of de Vriend and Koch²¹ for a fluid flux of $0.61 \text{ m}^3 \text{ s}^{-1}$. The experimental data correspond to the cross section E_0 for three different conditions of the tail gate, designated as T1-1, T1-2, and T1-3 cases. On the other hand, in Fig. 12(b), the radial profile of h/h_c is compared with the experimental data of de Vriend and Koch,²² corresponding to the cross section D_0 , for a fluid flux of $0.463 \text{ m}^3 \text{ s}^{-1}$. Overall, the experimental data somewhat depart from the computed radial free surface profiles. The deviations are primarily ascribed to the free surface instabilities, which hinder to accomplish an accurate measurement of the free surface profiles. However, in Fig. 12(b), the computed radial free surface profile has a satisfactory agreement with the experimental data for $Y \in [-0.5, 1]$.

C. Stress field

Let us first examine the behavior of radial shear stress, which can be obtained from Eq. (17). Importantly, the radial shear stress jointly depends on the local turbulent diffusivity and the gradient

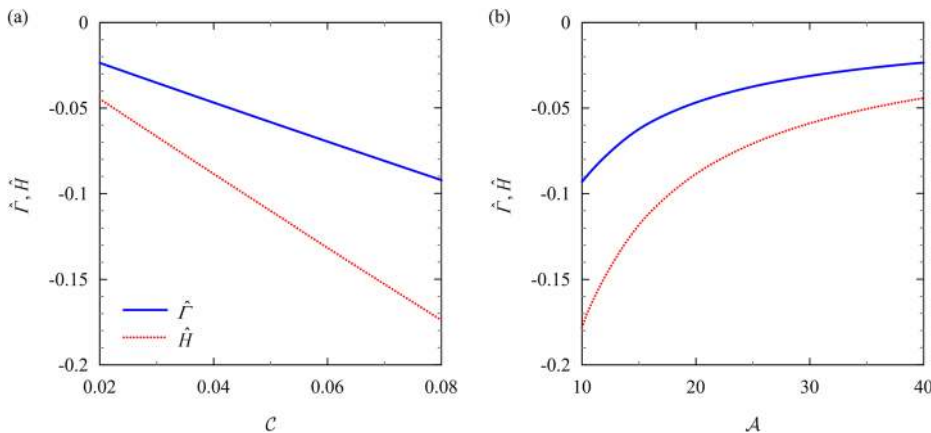


FIG. 10. Nondimensional radial circulation $\hat{\Gamma} [= \Gamma_\theta(b\langle U \rangle)^{-1}]$ and helicity $\hat{H} [= H(b\langle U \rangle^2)^{-1}]$ per unit azimuthal distance as a function of (a) curvature ratio $C (= b/r_c)$ and (b) aspect ratio $\mathcal{A} (= b/\langle h \rangle)$.

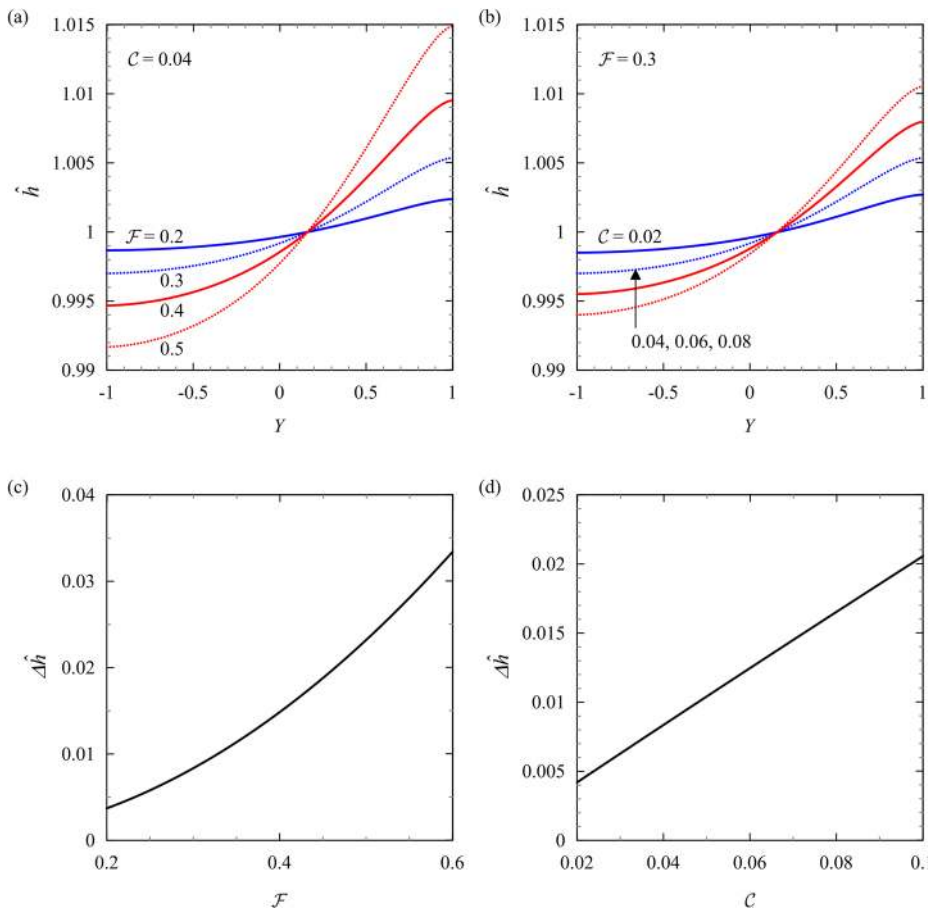


FIG. 11. Nondimensional radial free surface profiles \hat{h} ($=h/h_c$) for (a) flow Froude numbers $\mathcal{F} = 0.2, 0.3, 0.4,$ and 0.5 and (b) curvature ratios $C (=b/r_c) = 0.02, 0.04, 0.06,$ and 0.08 . Nondimensional superlevation $\Delta\hat{h}$ ($=\Delta h/h_c$) as a function of (c) flow Froude number \mathcal{F} and (d) curvature ratio C .

of radial velocity. Figure 13 illustrates the contours of nondimensional radial shear stress $\hat{\tau}_{rz} [= \tau_{rz}(\rho(U)^2)^{-1}]$ on the nondimensional YZ-plane for $C = 0.04$, $\lambda = 7$, and $A = 20$. The contours clearly demonstrate that at the mid-flow depth, the radial shear stress is primarily magnified toward the outer sidewall. In the near-bed flow zone, the radial shear stress is negative due to the radial motion of

fluid toward the inner sidewall (Fig. 6). However, away from the bed, the radial shear stress is positive because the radial motion of fluid is directed toward the outer sidewall. Close to the free surface, the radial shear stress becomes vanishingly small because the turbulent diffusivity diminishes toward the free surface. However, the radial velocity still persists at the free surface (see Figs. 6 and 7). At the

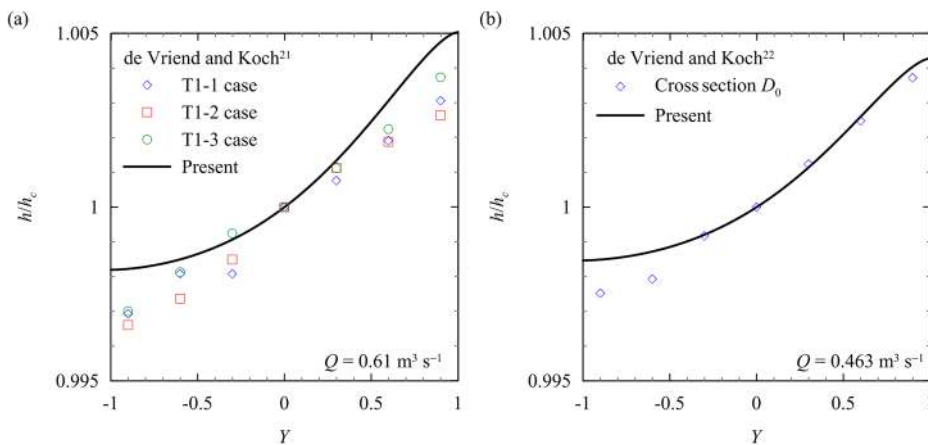


FIG. 12. Comparison of nondimensional radial free surface profiles with the experimental data for fluid fluxes Q of (a) $0.61 \text{ m}^3 \text{ s}^{-1}$ and (b) $0.463 \text{ m}^3 \text{ s}^{-1}$.

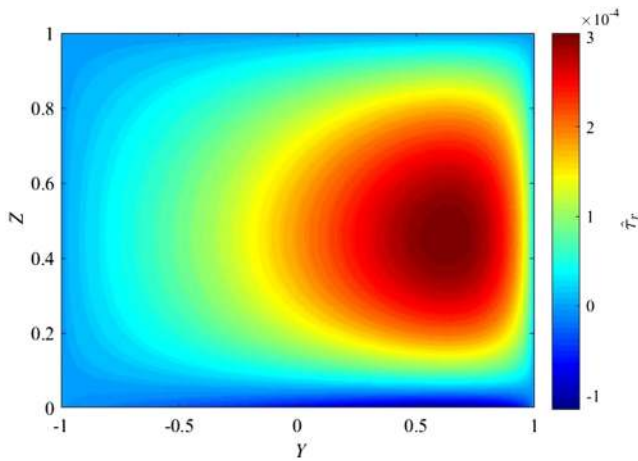


FIG. 13. Contours of nondimensional radial shear stress $\hat{\tau}_{rz} [= \tau_{rz}(\rho(U)^2)^{-1}]$ on the nondimensional YZ -plane for curvature ratio $C (=b/r_c) = 0.04$, reciprocal of the power-law exponent $\lambda = 7$, and aspect ratio $\mathcal{A} (=b/(h)) = 20$.

mid-flow depth, the radial shear stress is practically insignificantly close to the inner sidewall. On the other hand, it is substantially close to the outer sidewall owing to the skewed velocity filament, giving rise to nontrivial radial velocity (Fig. 6). However, in the

immediate proximity of the outer sidewall, the radial shear stress disappears.

The evolutions of the radial shear stress subjected to several key parameters can be further studied. The vertical profiles of nondimensional radial shear stress $\hat{\tau}_{rz}$ at the channel centerline ($Y = 0$) for different values of C , λ , and \mathcal{A} are depicted in Figs. 14(a)–14(c). For a given C , λ , and \mathcal{A} , the radial shear stress in the close proximity of the bed starts with a negative value since the local radial strain rate is essentially negative there. Then, it reduces (reduction in negative magnitude) with an increase in the vertical distance [Figs. 14(a)–14(c)], eventually becoming zero at a vertical distance, where the local radial velocity profile forms a protuberance [see Figs. 7(a)–7(c)]. As the vertical distance further increases, the radial shear stress enhances owing to the enhancement of turbulent diffusivity, becoming maximum approximately at the mid-flow depth, where the radial velocity switches over from a negative to positive value. Thereafter, the radial shear stress decreases with the vertical distance owing to a reduction in turbulent diffusivity and ultimately vanishes at the free surface [Figs. 14(a)–14(c)]. At a given vertical distance, the absolute magnitude of the radial shear stress grows with an increase in the curvature ratio due to an augmentation of the radial velocity arising from centrifugal acceleration [Fig. 14(a)]. The radial shear stress profiles, for different curvatures and aspect ratios, clearly show a pivoting point, located at $Z = 0.05$, which closely corresponds to the occurrence of protuberance in the radial velocity profile

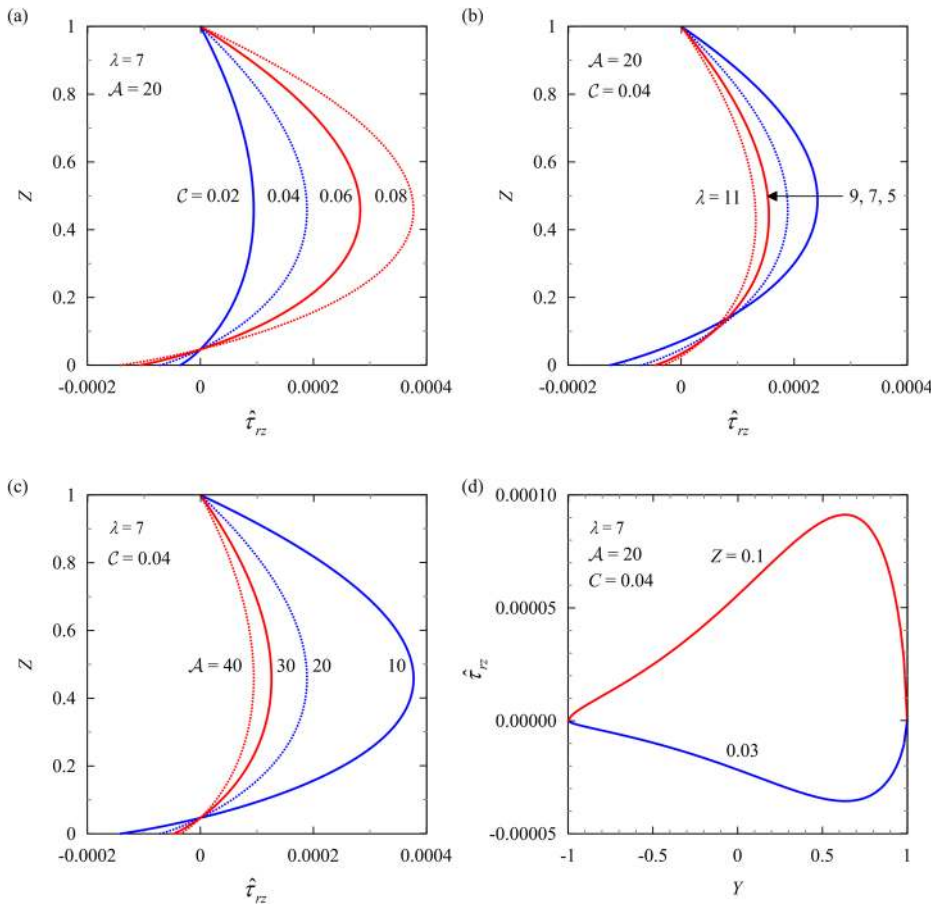


FIG. 14. Vertical profiles of nondimensional radial shear stress $\hat{\tau}_{rz} [= \tau_{rz}(\rho(U)^2)^{-1}]$ at the channel centerline for (a) curvature ratios $C (=b/r_c) = 0.02, 0.04, 0.06$, and 0.08 , (b) reciprocal of the power-law exponents $\lambda = 5, 7, 9$, and 11 , and (c) aspect ratios $\mathcal{A} (=b/(h)) = 10, 20, 30$, and 40 . (d) Radial profiles of nondimensional radial shear stress $\hat{\tau}_{rz}$ at nondimensional vertical distances $Z = 0.03$ and 0.1 .

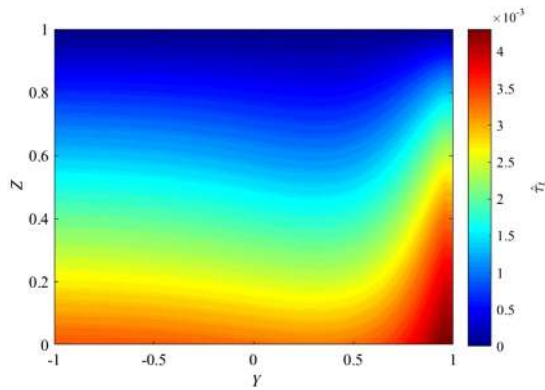


FIG. 15. Contours of nondimensional azimuthal shear stress $\hat{\tau}_{\theta z} [= \tau_{\theta z}(\rho(U)^2)^{-1}]$ on the nondimensional YZ-plane for the curvature ratio $C (=b/r_c) = 0.04$, reciprocal of the power-law exponent $\lambda = 7$, and aspect ratio $\mathcal{A} (=b/(h)) = 20$.

[Figs. 14(a)–14(c)]. Conversely, for different reciprocals of the power-law exponents, the pivoting point is not formed at the occurrence of protuberance in the radial velocity profile; rather, it is formed at $Z = 0.15$ [Fig. 14(b)]. At a given vertical distance, the

absolute magnitude of the radial shear stress increases with a decrease in the reciprocal of the power-law exponent [Fig. 14(b)]. Similar observation on the evolutions of the radial shear stress profiles is noticeable for different aspect ratios [Fig. 14(c)]. As the aspect ratio decreases, the radial shear stress becomes nontrivial owing to a sizable gradient of radial velocity. Figure 14(d) shows the radial profiles of nondimensional radial shear stress at two vertical distances $Z = 0.03$ and 0.1 , where the radial shear stress is directed toward the inner and outer sidewalls, respectively. The radial skew of the radial shear stress toward the outer sidewall is quite prominent from Fig. 14(d). Note that the absolute magnitudes of the radial shear stress, for $Z = 0.03$ and 0.1 , become maximum at $Y = 0.65$, while they are quite negligible in the immediate neighborhood of the sidewalls.

Now, we focus on the behavior of the azimuthal shear stress. The azimuthal shear stress at a given radial and vertical distances can be obtained from Eq. (23). In Fig. 15, the contours of nondimensional azimuthal shear stress $\hat{\tau}_{\theta z} [= \tau_{\theta z}(\rho(U)^2)^{-1}]$ on the nondimensional YZ-plane is shown for $C = 0.04$, $\lambda = 7$, and $\mathcal{A} = 20$. For a given vertical distance, the azimuthal shear stress slowly reduces as one moves toward the channel centerline owing to the redistribution of the primary flow momentum. However, for a given vertical distance, it increases as the radial distance increases beyond $Y = 0.5$.

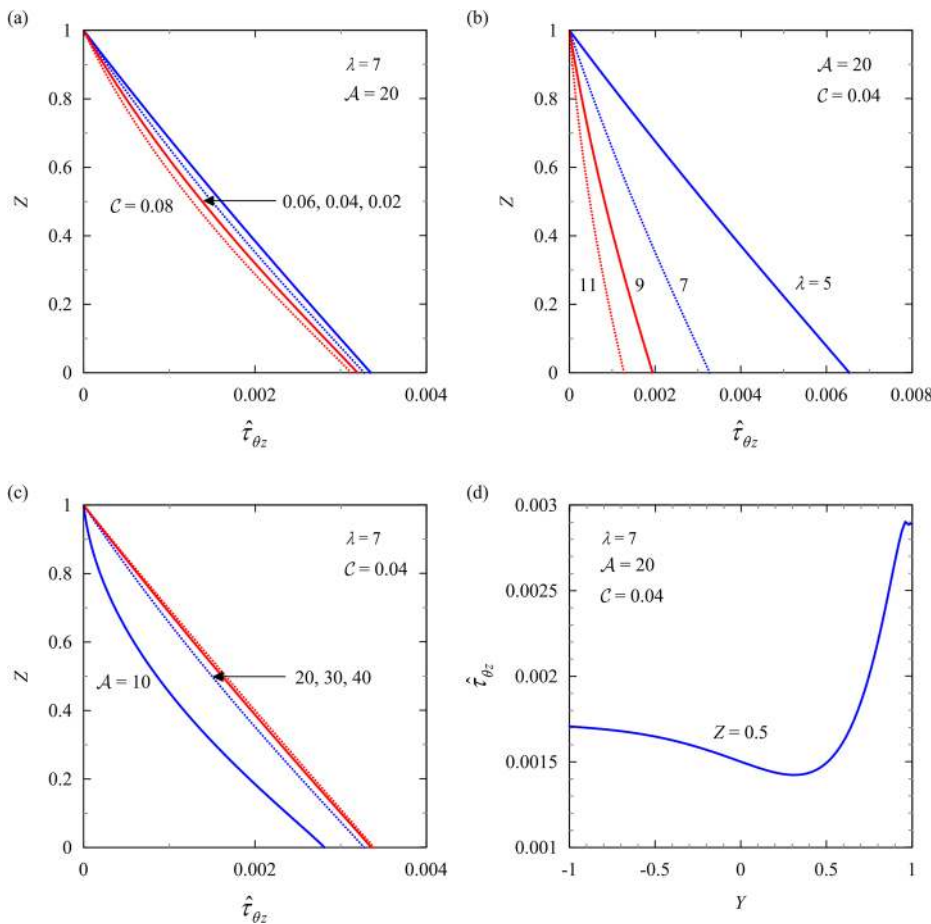


FIG. 16. Vertical profiles of nondimensional azimuthal shear stress $\hat{\tau}_{\theta z} [= \tau_{\theta z}(\rho(U)^2)^{-1}]$ at the channel centerline for (a) curvature ratios $C (=b/r_c) = 0.02, 0.04, 0.06, \text{ and } 0.08$, (b) reciprocal of the power-law exponents $\lambda = 5, 7, 9, \text{ and } 11$, and (c) aspect ratios $\mathcal{A} (=b/(h)) = 10, 20, 30, \text{ and } 40$. (d) Radial profiles of nondimensional azimuthal shear stress $\hat{\tau}_{\theta z}$ at nondimensional vertical distance $Z = 0.5$.

To study the sensitivity of the azimuthal shear stress to different key parameters, the vertical profiles of nondimensional azimuthal shear stress $\bar{\tau}_{\theta z}$ at the channel centerline ($Y = 0$) for different values of C , λ , and \mathcal{A} are depicted in Figs. 16(a)–16(c). For a given C , λ , and \mathcal{A} , the azimuthal shear stress distinguishingly maintains a nonlinear behavior induced by the curvilinear streamlines, having a maximum magnitude at the bed and a vanishing magnitude at the free surface. At a given vertical distance, it diminishes with an increase in the curvature ratio [Fig. 16(a)]. This is principally attributed to an increase in the damping function with the curvature ratio (see Sec. II E). In addition, the nonlinearity in the azimuthal shear stress profile increases with an increase in the curvature ratio. On the other hand, at a given vertical distance, the azimuthal shear stress reduces with an increase in the reciprocal of the power-law exponent [Fig. 16(b)]. Conversely, at a given vertical distance, it reduces with a reduction in the aspect ratio [Fig. 16(c)], which suggests that the azimuthal shear stress dampens more quickly for a lower aspect ratio ($\mathcal{A} = 10$). In essence, for larger aspect ratios exceeding $\mathcal{A} = 30$, the azimuthal shear stress profiles become nearly frozen, revealing the independency of the azimuthal shear stress profile on the aspect ratio. Note that the azimuthal shear stress profile for $\mathcal{A} = 10$ is highly nonlinear owing to the large damping function resulting from strong radial velocity. In Fig. 16(d), the radial profile of nondimensional azimuthal shear stress at $Z = 0.5$ is furnished. Starting from the inner sidewall ($Y = -1$), it slowly reduces with the radial distance owing to the reduction in primary flow momentum, attaining a minimum value at $Y = 0.3$, and then increases with the radial distance.

IV. CONCLUSIONS

This study sheds light on the hydrodynamics of weakly curved channels, solving analytically the boundary layer equations in three dimensions and employing the no-slip as well as a zero radial flux condition as the essential boundary conditions. The azimuthal shear stress is modeled by the Boussinesq conjecture for a turbulent flow. On the other hand, the radial shear stress is evaluated by applying the isotropic notion of turbulence. The radial slope correction factor in conjunction with the damping function for the azimuthal shear stress is introduced in the theoretical analysis to account for the stress term in the radial momentum balance and the skewing of the primary flow momentum induced by the curvilinear streamlines, respectively.

The azimuthal velocity scaled by its depth-averaged value follows the power-law, while the depth-averaged azimuthal velocity scaled by the depth-averaged centerline azimuthal velocity preserves a quadratic-cum-exponential law. The velocity field reveals that the Boussinesq and Coriolis coefficients in a weakly curved channel flow surpass their respective upper limits in a straight channel flow. The radial velocity is quite strong just above the bed and at the free surface, at a radial distance that closely corresponds to the radial location of the maximum depth-averaged azimuthal velocity. By contrast, it is weaker near the sidewalls owing to the no-slip. The absolute magnitude of the radial velocity, for a given spatial location, grows with the curvature ratio as a result of the intensified centrifugal acceleration. The vertical profiles of radial velocity, for different curvature ratios, clearly depict a pivoting point, while those, for different reciprocals of the power-law exponents exceeding seven, become frozen above mid-flow depth. The pivoting point of the

radial velocity profiles for different reciprocals of the power-law exponents occurs approximately at a vertical distance of one-third of the flow depth. The absolute magnitude of the radial velocity, for a given spatial location, declines with an increase in the aspect ratio. For a large aspect ratio exceeding 30, the radial velocity profiles become quasifrozen, having the pivoting point approximately located at the mid-flow depth.

In the near-bed flow zone, the azimuthal vorticity is substantial due to the steep gradients of the radial and vertical velocities in secondary current. In addition, the azimuthal vorticity, for a given vertical distance, is larger toward the outer sidewall than toward the inner sidewall. On the other hand, the azimuthal vorticity, for a given radial distance, reduces with an increase in the vertical distance. The absolute magnitudes of the flow circulation about the azimuthal axis and the flow helicity intensify with an increase in the curvature ratio, whereas they reduce as the aspect ratio increases.

For a given radial distance, the free surface level diminishes with an increase in the flow Froude number close to the inner sidewall, whereas it increases close to the outer sidewall. The radial free surface profiles depict a quicker evolution with the flow Froude number than with the curvature ratio. The superelevation increases nonlinearly with the flow Froude number and linearly with the curvature ratio.

The strengthening of the radial shear stress occurs toward the outer sidewall at the mid-flow depth. In the near-bed flow zone, the radial shear stress is negative owing to the inward motion of fluid, while away from the bed, it is positive. The absolute magnitude of the radial shear stress, at a given spatial location, increases with an increase in the curvature ratio owing to the large gradient of the radial velocity. The vertical profiles of radial shear stress, for different curvatures and aspect ratios, show a pivoting point in each profile that closely corresponds to the occurrence of protuberance in the radial velocity profile. On the other hand, for different reciprocals of the power-law exponents, the pivoting point does not correspond to the position of protuberance in the radial velocity profile. The absolute magnitude of the radial shear stress, at a given spatial location, strengthens with a reduction in the reciprocal of the power-law exponent and aspect ratio.

The azimuthal shear stress, at a given spatial location, gradually dampens toward the channel centerline, resulting from the redistribution of the primary flow momentum. On the other hand, the azimuthal shear stress, at a given spatial location, reduces with an increase in the curvature ratio owing to an increased damping function. In addition, the azimuthal shear stress, at a given spatial location, reduces with the reciprocal of the power-law exponent, while it reduces with a decrease in the aspect ratio. The vertical profiles of azimuthal shear stress become frozen for larger aspect ratios exceeding 30. However, for a low aspect ratio equaling ten, the azimuthal shear stress profile becomes nonlinear owing to the substantial damping of the primary flow momentum, originating from the large radial velocity.

In essence, this study essentially addresses the sensitivity of the helicoidal flow structure to key parameters, such as the channel curvature ratio, channel aspect ratio, and reciprocal of power-law exponent, without considering the depth-averaged assumptions. However, this study does not consider the effects of flow separation, which arises in a strongly curved channel flow. Despite plausible assumptions, this study thus offers a promising analytical model

of flow through a weakly curved channel, advancing the current state-of-the-art.

ACKNOWLEDGMENTS

S.D. acknowledges the JC Bose Fellowship Award (JBD) for pursuing this work.

REFERENCES

- ¹W. R. Dean, "Note on the motion of fluid in a curved pipe," *Philos. Mag.* **4**, 208–223 (1927).
- ²W. R. Dean, "The stream-line motion of fluid in a curved pipe," *Philos. Mag.* **5**, 673–695 (1928).
- ³A. Kalpakli Vester, R. Örlü, and P. H. Alfredsson, "Turbulent flows in curved pipes: Recent advances in experiments and simulations," *Appl. Mech. Rev.* **68**, 050802 (2016).
- ⁴A. O. Demuren and W. Rodi, "Calculation of flow and pollutant dispersion in meandering channels," *J. Fluid Mech.* **172**, 63–92 (1986).
- ⁵I. Nezu and H. Nakagawa, *Turbulence in Open-Channel Flows* (Balkema, Rotterdam, 1993).
- ⁶S. Dey, *Fluvial Hydrodynamics: Hydrodynamic and Sediment Transport Phenomena* (Springer-Verlag, Berlin, Germany, 2014).
- ⁷C. A. Mockmore, "Flow around bends in stable channels," *Trans. Am. Soc. Civ. Eng.* **109**, 593–618 (1944).
- ⁸A. Shukry, "Flow around bends in an open flume," *Proc. Am. Soc. Civ. Eng.* **75**, 713–741 (1949).
- ⁹H. A. Einstein and J. A. Harder, "Velocity distribution and the boundary layer at channel bends," *Trans., Am. Geophys. Union* **35**, 114–120 (1954).
- ¹⁰W. F. Tanner, "Spiral flow in rivers, shallow seas, dust devils, and models," *Science* **139**, 41–42 (1963).
- ¹¹I. L. Rozovskii, *Flow of Water in Bends in Open Channels* (Academy of Sciences of the Ukrainian Soviet Socialist Republic, Kiev, 1957).
- ¹²M. Falcón, "Secondary flow in curved open channels," *Annu. Rev. Fluid Mech.* **16**, 179–193 (1984).
- ¹³H. Kikkawa, S. Ikeda, and A. Kitagawa, "Flow and bed topography in curved open channels," *J. Hydraul. Div., Am. Soc. Civ. Eng.* **102**, 1327–1342 (1976).
- ¹⁴M. Falcón Ascanio and J. F. Kennedy, "Flow in alluvial-river curves," *J. Fluid Mech.* **133**, 1–16 (1983).
- ¹⁵S. Ikeda and T. Nishimura, "Flow and bed profile in meandering sand-silt rivers," *J. Hydraul. Eng.* **112**, 562–579 (1986).
- ¹⁶A. J. Odgaard, "River-meander model. I: Development," *J. Hydraul. Eng.* **115**, 1433–1450 (1989).
- ¹⁷S. Ikeda, M. Yamasaka, and J. F. Kennedy, "Three-dimensional fully developed shallow-water flow in mildly curved bends," *Fluid Dyn. Res.* **6**, 155–173 (1990).
- ¹⁸H. J. de Vriend, "A mathematical model of steady flow in curved shallow channels," *J. Hydraul. Res.* **15**, 37–54 (1977).
- ¹⁹K.-C. Yeh and J. F. Kennedy, "Moment model of nonuniform channel-bend flow. I: Fixed beds," *J. Hydraul. Eng.* **119**, 776–795 (1993).
- ²⁰J. C. Bathurst, C. R. Thorne, and R. D. Hey, "Direct measurements of secondary currents in river bends," *Nature* **269**, 504–506 (1977).
- ²¹H. J. de Vriend and F. G. Koch, "Flow of water in a curved open channel with a fixed plane bed," Report on experimental and theoretical investigations, R 657-V/M 1415 Part I, Delft University of Technology, 1977.
- ²²H. J. de Vriend and F. G. Koch, "Flow of water in a curved open channel with a fixed uneven bed," Report on experimental and theoretical investigations, R 657-VI/M 1415 Part II, Delft University of Technology, 1978.
- ²³C. Zimmerman and J. F. Kennedy, "Transverse bed slopes in curved alluvial streams," *J. Hydraul. Div., Am. Soc. Civ. Eng.* **104**, 33–48 (1978).
- ²⁴H. J. de Vriend, "Steady flow in shallow channel bends," Ph.D. thesis, Department of Hydraulic Engineering, Delft University of Technology, 1981.
- ²⁵C. R. Thorne, L. W. Zevenbergen, J. C. Pitlick, S. Rais, J. B. Bradley, and P. Y. Julien, "Direct measurements of secondary currents in a meandering sand-bed river," *Nature* **315**, 746–747 (1985).
- ²⁶A. J. Odgaard and M. A. Bergs, "Flow processes in a curved alluvial channel," *Water Resour. Res.* **24**, 45–56, <https://doi.org/10.1029/wr024i001p00045> (1988).
- ²⁷K. Blanckaert and H. J. de Vriend, "Turbulence characteristics in sharp open-channel bends," *Phys. Fluids* **17**, 055102 (2005).
- ²⁸M. A. Leschziner and W. Rodi, "Calculation of strongly curved open channel flow," *J. Hydraul. Div., Am. Soc. Civ. Eng.* **105**, 1297–1314 (1979).
- ²⁹H. J. de Vriend, "Velocity redistribution in curved rectangular channels," *J. Fluid Mech.* **107**, 423–439 (1981).
- ³⁰J. Ye and J. A. Mccorquodale, "Simulation of curved open-channel flows by 3D hydrodynamic model," *J. Hydraul. Eng.* **124**, 687–698 (1998).
- ³¹R. Booij, "Measurements and large eddy simulations of the flows in some curved flumes," *J. Turbul.* **4**, 8 (2003).
- ³²W. van Balen, W. S. J. Uijttewaai, and K. Blanckaert, "Large-eddy simulation of a curved open-channel flow over topography," *Phys. Fluids* **22**, 075108 (2010).
- ³³Y.-C. Jin and P. M. Steffler, "Predicting flow in curved open channels by depth-averaged method," *J. Hydraul. Eng.* **119**, 109–124 (1993).
- ³⁴A. A. Kassem and M. H. Chaudhry, "Numerical modeling of bed evolution in channel bends," *J. Hydraul. Eng.* **128**, 507–514 (2002).
- ³⁵P. K. Kitanidis and J. F. Kennedy, "Secondary current and river-meander formation," *J. Fluid Mech.* **144**, 217–229 (1984).
- ³⁶S. B. Pope, *Turbulent Flows* (Cambridge University Press, Cambridge, 2000).
- ³⁷H. Schlichting, *Boundary Layer Theory* (McGraw-Hill, New York, 1979).
- ³⁸H. K. Moffatt, "The degree of knottedness of tangled vortex lines," *J. Fluid Mech.* **35**, 117–129 (1969).